IOP Publishing | International Atomic Energy Agency Nuclear Fusion

Nucl. Fusion **61** (2021) 036006 (20pp) https://doi.org/10.1088/1741-4326/abd09d

Current profile and normalized beta control via feedback linearization and Lyapunov techniques

Andres Pajares and Eugenio Schuster

Department of Mechanical Engineering and Mechanics, Lehigh University, Bethlehem, PA 18015, United States of America

E-mail: andres.pajares@lehigh.edu

Received 31 August 2020, revised 17 November 2020
Accepted for publication 4 December 2020
Published 22 January 2021

Abstract

Simultaneous control of the current profile and normalized plasma beta is an essential control problem in the development of advanced tokamak scenarios. However, this control problem is especially challenging due to the nonlinear nature of the current, heat, and particle transport dynamics, as well as the difficulty to understand and accurately model such processes. In this work, a nonlinear, robust, model-based controller for the simultaneous regulation of the current profile and normalized beta has been designed using feedback linearization and Lyapunov redesign techniques. Feedback linearization avoids approximate linearization of the plasma dynamics, retaining the original physics content of the model. Moreover, the use of Lyapunov redesign techniques makes the controller robust against the uncertainties arising during the modeling process. The controller's performance in the presence of unknown dynamics is tested in nonlinear, one-dimensional simulations using the Control Oriented Transport SIMulator (COTSIM) code, which employs plasma models that are significantly more complex than those employed for control synthesis.

Keywords: current profile control, tokamak-plasma control, nonlinear plasma simulation

(Some figures may appear in colour only in the online journal)

1. Introduction

ITER's main mission is to demonstrate the feasibility of nuclear fusion as a sustainable, economically attractive means of energy production. Generally speaking, there are two types of plasma scenarios through which such goal may be attained: inductively-driven scenarios, characterized by a relatively high plasma current, high inductive-current fraction, and short pulse duration, and advanced tokamak (AT) scenarios, characterized by a relatively low plasma current, high non-inductive-current fractions, and longer pulses [1]. Whereas inductive scenarios are in principle easier to reproduce and operate, the possibility of achieving longer (ideally, steady-state) pulses by means of AT scenarios makes the latter specially attractive. However, there are several challenges associated with the AT path. First, the positive scaling of the energy confinement time, τ_E, with the plasma current, I_p, requires that AT scenarios exhibit particularly good confinement conditions in order to achieve high enough Q gains (where Q is the ratio of fusion power to auxiliary power). Second, a key feature to access steady-state (or quasi-steady-state) conditions is the need for a high bootstrap-current fraction [2], which is highly dependent on the pressure gradient and total current profiles. Finally, this coupling between the pressure gradient (which is sometimes increased at low or negative magnetic-shear, $s \triangleq \frac{r}{q}\frac{dq}{dr}$, where q is the safety factor and r is the minor radius) and the bootstrap current (which is peaked off-axis and, therefore, contributes to reducing s) may drive the normalized plasma beta, β_N, towards too high values. This may trigger magnetohydrodynamic (MHD) instabilities that substantially deteriorate the plasma performance and, in the worst case, may terminate the confined plasma. Therefore, due to all these challenges,

AT scenarios may significantly benefit from active feedback (FB) control to maintain a desired current profile and/or β_N evolutions that maximize the plasma confinement and bootstrap current fraction.

Significant effort has been carried out within the fusion community to develop control algorithms for the regulation of the current profile and β_N. First steps towards current profile control can be found in [3] for Tore Supra (now WEST), [4] for JT-60, or [5] for DIII-D. In these pieces of work, non-model-based techniques were employed together with linear control designs. Subsequent model-based work can be found in [6–12], where different control design techniques such as optimal control, robust control, and model predictive control were employed. A quite common approach to model-based current-profile + β_N control is using an approximately linearized version of the system dynamics at some point during the control design. This makes the control synthesis tractable by reducing the mathematical complexity of the model, but with the inevitable consequence of losing some physics information. Pieces of work that propose fully nonlinear control designs can be found, for example, in [13] (where backstepping techniques are employed), in [14] (in which Lyapunov techniques are applied), or in [15] (where passivity-based techniques are utilized). Also, although some of the aforementioned pieces of work do study and assess the robustness of the proposed algorithms against uncertain and unmodeled dynamics, robust-control techniques are not commonly employed. Based on linearized versions of the system dynamics, a controller that uses linear robust-control techniques is proposed in [16].

In this work, a model-based, nonlinear-robust controller is synthesized for simultaneous current-profile + β_N control by means of FB linearization and Lyapunov redesign techniques [17]. To the authors' best knowledge, this is the first controller for the current profile in tokamaks that uses nonlinear-robust control techniques. The control-oriented model of the current-profile + β_N dynamics employed for control design is similar to the one employed in previous work [18]. By means of FB linearization, a nonlinear controller for current-profile regulation can be designed without recurring to approximate linearization techniques. This removes the natural limitations imposed by a control design based on approximate linearization and/or linear techniques. First steps towards FB-linearization-based current-profile control (without simultaneous β_N control) can be found in [19, 20]. The controller proposed in the present work employs the total plasma current, I_p, modulation of the neutral beam injection (NBI) powers, and modulation of the electron-cyclotron (EC) power as the available actuators for control. First, nonlinear, robust control laws are designed based on Lyapunov theory and Lyapunov redesign techniques for the total injected power, P_tot, to control β_N, and for I_p to control the safety factor at the plasma edge, q_edge. These two control laws for P_tot and I_p can be easily embedded in the FB-linearization control scheme. Second, a study is carried out to analyze under what conditions the current-profile subsystem is FB linearizable, and if so, how many spatial locations of the current profile can be controlled in conjunction with β_N by means of FB linearization. It will be shown that the nominal system is in fact FB linearizable as long as the auxiliary sources have different enough current-deposition profiles. Such analysis allows for a very intuitive assessment of the current-profile + β_N control capability within a tokamak. Third, a FB-linearization nominal control law is synthesized to control the current profile at the interior nodes by means of the NBI and EC powers, assuming no uncertainty. Finally, the FB-linearization nominal control law is nonlinearly robustified by means of Lyapunov redesign techniques, so that the controller is robust against unmodeled dynamics in the evolution of n_e and T_e. The uncertainties in n_e and T_e lead in turn to uncertainties in the plasma resistivity and current deposition from non-inductive sources, which play a fundamental role in the current-profile dynamics. Such model uncertainties may arise from our limited knowledge of the complex physical processes impacting transport in a tokamak plasma such as MHD activity, fast-ion dynamics, and impurity dynamics among others. These model uncertainties may also arise from a decision of not explicitly including all the physics impacting the evolution of n_e and T_e in the model employed for control synthesis in order to keep the control-design problem tractable.

The paper is organized as follows. The nonlinear plasma model employed for control synthesis is briefly described in section 2. The current profile + β_N control algorithm is synthesized in section 3. The controller is tested in one-dimensional (1D) simulations using the Control Oriented Transport SIMulation (COTSIM) code in section 4 based on plasma response models more complex than those used for control synthesis. Finally, some conclusions and possible future work are stated in section 5. Appendices are provided with details of the model derivation (appendix A) and to cover the basics of the Lyapunov stability theory (appendix B) and Lyapunov redesign techniques (appendix C).

2. Plasma model for control synthesis

2.1. Nominal plasma model

The q profile measures the pitch of the magnetic field lines in a tokamak. It is given by

$$q(\hat{\rho},t) = -\frac{B_{\phi,0}\rho}{\partial\psi(\rho,t)/\partial\rho} = -\frac{\rho_b^2 B_{\phi,0}\hat{\rho}}{\partial\psi(\hat{\rho},t)/\partial\hat{\rho}}, \tag{1}$$

where $B_{\phi,0}$ is the vacuum magnetic field at the magnetic axis, ρ is the mean effective minor radius, ρ_b is the mean effective minor radius of the last-closed magnetic-flux surface, $\hat{\rho} \triangleq \rho/\rho_b$ is the normalized mean effective minor radius, which is employed as the spatial coordinate in this work, and ψ is the poloidal stream function. The time evolution of ψ is given by the magnetic diffusion equation (MDE) [21],

$$\frac{\partial\psi(\hat{\rho},t)}{\partial t} = \frac{\eta(\hat{\rho},t)}{\mu_0\rho_b^2\hat{F}(\hat{\rho})^2\hat{\rho}}\frac{\partial}{\partial\hat{\rho}}\left(\hat{\rho}\hat{F}(\hat{\rho})\hat{G}(\hat{\rho})\hat{H}(\hat{\rho})\frac{\partial\psi(\hat{\rho},t)}{\partial\hat{\rho}}\right) + \eta(\hat{\rho},t)R_0\hat{H}(\hat{\rho})j_\mathrm{ni}(\hat{\rho},t), \tag{2}$$

where t is the time, η is the plasma resistivity, μ_0 is the vacuum permeability, $\hat{F}$, $\hat{G}$ and $\hat{H}$ are geometric factors that correspond to a particular plasma equilibrium, R_0 is the tokamak

major radius, and $j_{\rm ni} \triangleq \langle \vec{j}_{\rm ni} \cdot \vec{B} \rangle / B_{\phi,0}$ is the contribution from non-inductive sources ($\vec{j}_{\rm ni}$ is the non-inductive plasma current density, $\vec{B}$ is the magnetic field, and $\langle \cdot \rangle$ denotes a flux-surface average). The boundary conditions associated with (2) are given by

$$\left.\frac{\partial \psi}{\partial \hat{\rho}}\right|_{\hat{\rho}=0} = 0, \qquad \left.\frac{\partial \psi}{\partial \hat{\rho}}\right|_{\hat{\rho}=1} = -\frac{\mu_0 R_0}{2\pi \hat{G}(\hat{\rho}=1)\hat{H}(\hat{\rho}=1)} I_{\rm p}(t) = -k_{I_{\rm p}} I_{\rm p}(t), \tag{3}$$

where $\hat{G}$ is a geometric factor, and $k_{I_{\rm p}} \triangleq \mu_0 R_0/(2\pi \hat{G}(\hat{\rho}=1)\hat{H}(\hat{\rho}=1))$ is a constant.

Models for η and $j_{\rm ni}$ that depend on the electron temperature, $T_{\rm e}$, and electron density, $n_{\rm e}$, are employed in this work. Such models are given by

$$\eta(\hat{\rho},t) = \frac{Z_{\rm eff} k_{\rm sp}(\hat{\rho})}{T_{\rm e}(\hat{\rho},t)^{3/2}}, \quad j_{\rm ni}(\hat{\rho},t) = j_{\rm aux}(\hat{\rho},t) + j_{\rm BS}(\hat{\rho},t), \tag{4}$$

$$j_{\rm aux}(\hat{\rho},t) = \sum_{i=1}^{i=N_{\rm NBI}} j^{\rm dep}_{{\rm NBI},i}(\hat{\rho}) \frac{T_{\rm e}(\hat{\rho},t)^{\lambda_{\rm NBI}}}{n_{\rm e}(\hat{\rho},t)} P_{{\rm NBI},i}(t) + j^{\rm dep}_{\rm EC}(\hat{\rho}) \frac{T_{\rm e}(\hat{\rho},t)^{\lambda_{\rm EC}}}{n_{\rm e}(\hat{\rho},t)} P_{\rm EC}(t), \tag{5}$$

$$j_{\rm BS}(\hat{\rho},t) = \frac{R_0}{\hat{F}(\hat{\rho})} \left(\frac{\partial \psi(\hat{\rho},t)}{\partial \hat{\rho}}\right)^{-1} \left[2\mathcal{L}_{31}(\hat{\rho}) T_{\rm e}(\hat{\rho},t) \frac{\partial n_{\rm e}(\hat{\rho},t)}{\partial \hat{\rho}} + (2\mathcal{L}_{31}(\hat{\rho}) + \mathcal{L}_{32}(\hat{\rho}) + \alpha(\hat{\rho})\mathcal{L}_{34}(\hat{\rho})) n_{\rm e}(\hat{\rho},t) \times \frac{\partial T_{\rm e}(\hat{\rho},t)}{\partial \hat{\rho}} \right], \tag{6}$$

where $Z_{\rm eff}$ is the effective atomic number of the plasma ions, $j_{\rm aux}$ and j_{BS} are, respectively, the auxiliary sources and bootstrap current contributions to the total non-inductive current, $k_{\rm sp}$, $j^{\rm dep}_{{\rm NBI},i}$ and $j^{\rm dep}_{\rm EC}$ are spatial profiles, $\lambda_{\rm NBI}$ and $\lambda_{\rm EC}$ are constant parameters that characterize the current-drive efficiency of the auxiliary sources, $P_{{\rm NBI},i}$, for $i = 1, \ldots, N_{\rm NBI}$ ($N_{\rm NBI}$ is the total number of NBI sources), are the individual NBI powers, $P_{\rm EC}$ is the total EC power, and $\mathcal{L}_{31}$, $\mathcal{L}_{32}$, $\mathcal{L}_{34}$, and α are spatial profiles corresponding to a particular magnetic equilibrium [22]. This simplified bootstrap-current model assumes a tight coupling between the ion and electron species (i.e., $T_{\rm i} = c_{\rm T} T_{\rm e}$ and $n_{\rm i} = c_n n_{\rm e}$). In particular, the expression in (6) assumes $c_{\rm T} = c_n = 1$.

To close the MDE model (1)–(6), control-oriented models for $T_{\rm e}$ and $n_{\rm e}$ are employed by exploiting the difference in dynamical timescales between kinetic and magnetic variables in a tokamak plasma. Thus, $T_{\rm e}$ and $n_{\rm e}$ are assumed to be infinitely fast (i.e., no dynamics) in the magnetic timescale and to directly scale with the inputs $I_{\rm p}$, total power, $P_{\rm tot}$, and line-average electron density, $\bar{n}_{\rm e}$, as

$$T_{\rm e}(\hat{\rho},t) = T^{\rm prof}_{\rm e}(\hat{\rho}) I_{\rm p}(t)^{\gamma} P_{\rm tot}(t)^{\epsilon} \bar{n}_{\rm e}(t)^{\zeta}, \tag{7}$$

$$n_{\rm e}(\hat{\rho},t) = n^{\rm prof}_{\rm e}(\hat{\rho}) \bar{n}_{\rm e}(t), \tag{8}$$

where γ, ϵ and ζ are constant parameters, and $T^{\rm prof}_{\rm e}$ and $n^{\rm prof}_{\rm e}$ are spatial profiles. More details about these models can be found in [18].

The dynamics of the plasma total energy, W, is modeled as

$$\frac{{\rm d}W(t)}{{\rm d}t} = -\frac{W(t)}{\tau_{\rm E}(t)} + P_{\rm tot}(t), \tag{9}$$

where $\tau_{\rm E}$ is the energy confinement time, which is estimated using the IPB98(y,2) scaling,

$$\tau_{\rm E}(t) = 0.0562 H_H(t) I_{\rm p}(t)^{0.93} B_{\rm T}^{0.15} R_0^{1.97} M^{0.19} \epsilon^{0.58} \times \bar{n}_{\rm e,19}(t)^{0.41} \kappa^{0.78} P_{\rm tot}(t)^{-0.69}, \tag{10}$$

where H_H is the so-called H-factor, $B_{\rm T}$ is the toroidal magnetic field, M is the plasma effective mass in amu, $\epsilon \triangleq a/R_0$ is the inverse aspect ratio, a is the tokamak minor radius, $\bar{n}_{\rm e,19}$ is the line-average electron density in 10^{19} m^{-3}, and κ is the plasma elongation at the 95% flux surface/separatrix. It is assumed that

$$P_{\rm tot} = \sum_{i=1}^{i=N_{\rm NBI}} P_{{\rm NBI},i} + P_{\rm EC}, \tag{11}$$

i.e., other sources of heating such as fusion heating, ohmic heating or radiative heating are neglected when compared with the heating by the auxiliary sources. This simplifying assumption is well justified in many present-device AT-scenario plasmas in which the fusion heating is virtually zero, whereas the ohmic and radiative heating are significantly smaller than the auxiliary heating during most of the discharge. More importantly, the control-synthesis model needs to primarily capture the response of the controlled variable (e.g., W) to the actuator mechanisms (e.g., NBI and ECH) while all the other uncontrollable inputs can be considered external disturbances. These and other simplifying assumptions like the one adopted for the bootstrap current above are made only to facilitate the control-synthesis procedure. The level of simplification adopted for the control-synthesis model usually involves an iterative process, where the assessment of the control performance in closed-loop simulation studies dictates the need for more model complexity and accuracy followed by control redesign. As it will be pointed out later in section 4, the simulation studies are based on more sophisticated models that avoid these simplifying assumptions.

2.2. Uncertainty modeling

One of the main issues when dealing with tokamak-plasma control problems is the inherent uncertainty existing in the modeling process of such a complex dynamical system. For example, as of now, existing theories can explain certain aspects of the plasma transport in a tokamak, but much of the phenomena explaining transport processes is still not totally understood. Moreover, there is only a certain degree of model complexity that can be handled for control synthesis. In this work, the modeling approach is based on the use of control-oriented models with the addition of uncertainty terms providing a measure of the unknown or neglected dynamics. The goal

of this modeling approach is to guarantee performance metrics of the controller within predefined bounds of the model uncertainties.

As a result, the dynamical models for T_e and n_e in (7) and (8) are modified as

$$\begin{aligned} T_e &= T_e^{\text{prof}}(\hat{\rho}) I_p(t)^{\gamma} P_{\text{tot}}(t)^{\epsilon} \bar{n}_e(t)^{\zeta} + \delta_{T_e}(\hat{\rho}, t), \; n_e \\ &= n_e^{\text{prof}}(\hat{\rho}) \bar{n}_e(t) + \delta_{n_e}(\hat{\rho}, t), \end{aligned} \tag{12}$$

where δ_{T_e} and δ_{n_e} are uncertain terms that model lack of physical knowledge and/or deviations in the modeled T_e and n_e evolutions. Although δ_{T_e} and δ_{n_e} are unknown, bounds for them can be estimated based on experimental and physical constraints. Because η and j_{ni} are functions of T_e and n_e, they can be written as

$$\begin{aligned} \eta(\hat{\rho}, t) &= \eta^{\text{nom}}(\hat{\rho}, t) + \delta_{\eta}(\hat{\rho}, t), \\ j_{\text{ni}}(\hat{\rho}, t) &= j_{\text{ni}}^{\text{nom}}(\hat{\rho}, t) + \delta_{j_{\text{ni}}}(\hat{\rho}, t), \end{aligned} \tag{13}$$

where η^{nom} and $j_{\text{ni}}^{\text{nom}}$ are given by (4)–(6), and δ_{η} and $\delta_{j_{\text{ni}}}$ are uncertain terms for which a bound can be estimated because they are directly related to δ_{T_e} and δ_{n_e}. The MDE, equation (2), can be rewritten as

$$\begin{aligned} \frac{\partial \psi(\hat{\rho}, t)}{\partial t} &= \frac{\eta^{\text{nom}}(\hat{\rho}, t)}{\mu_0 \rho_b^2 \hat{F}(\hat{\rho})^2 \hat{\rho}} \frac{\partial}{\partial \hat{\rho}} \left(\hat{\rho} D_{\psi}(\hat{\rho}) \frac{\partial \psi(\hat{\rho}, t)}{\partial \hat{\rho}} \right) \\ &\quad + \eta^{\text{nom}}(\hat{\rho}, t) R_0 \hat{H}(\hat{\rho}) j_{\text{ni}}^{\text{nom}}(\hat{\rho}, t) + \delta_{\psi}(\hat{\rho}, t), \end{aligned} \tag{14}$$

where $D_{\psi} \triangleq \hat{F} \hat{G} \hat{H}$, and δ_{ψ} is an uncertain term given by

$$\begin{aligned} \delta_{\psi}(\hat{\rho}, t) &= \frac{\delta_{\eta}(\hat{\rho}, t)}{\mu_0 \rho_b^2 \hat{F}(\hat{\rho})^2 \hat{\rho}} \frac{\partial}{\partial \hat{\rho}} \left(\hat{\rho} D_{\psi}(\hat{\rho}) \frac{\partial \psi(\hat{\rho}, t)}{\partial \hat{\rho}} \right) \\ &\quad + R_0 \hat{H}(\hat{\rho}) \left(\eta^{\text{nom}}(\hat{\rho}, t) \delta_{j_{\text{ni}}}(\hat{\rho}, t) \right. \\ &\quad \left. + j_{\text{ni}}^{\text{nom}}(\hat{\rho}, t) \delta_{\eta}(\hat{\rho}, t) + \delta_{\eta}(\hat{\rho}, t) \delta_{j_{\text{ni}}}(\hat{\rho}, t) \right), \end{aligned} \tag{15}$$

for which a bound can be estimated from δ_{η}, $\delta_{j_{\text{ni}}}$, the corresponding model parameters and profiles in equation (15), and the real-time estimation of the ψ profile.

The H-factor in equation (10) is also considered uncertain to reflect unknown changes in confinement that may happen during operation. It is modeled as

$$H_H(t) = H_H^{\text{nom}} + \delta_{H_H}(t), \tag{16}$$

where H_H^{nom} is a known constant, and δ_{H_H} is a bounded, uncertain term. The W-subsystem dynamics (9) can be rewritten as

$$\frac{\mathrm{d}W}{\mathrm{d}t} = -\frac{W}{\tau_E^{\text{nom}}} + P_{\text{tot}} + \delta_W, \tag{17}$$

where the dependence on t has been dropped in all variables to ease notation, τ_E^{nom} is the value of τ_E when $\delta_{H_H} = 0$, and δ_W is an uncertain term given by

$$\delta_W = \frac{W}{\tau_E^{\text{nom}}} - \frac{W}{\frac{H_H^{\text{nom}} + \delta_{H_H}(t)}{H_H^{\text{nom}}} \tau_E^{\text{nom}}}, \tag{18}$$

for which a bound can be estimated from δ_{H_H} and a real-time estimation of W.

Finally, it is assumed that the parameter k_{I_p} in (3) is not well known for control-synthesis purposes, and only a constant estimate, $k_{I_p}^*$, is available.

2.3. Uncertain plasma model

Introducing the definition of the poloidal flux gradient, $\theta \triangleq \partial \psi / \partial \hat{\rho}$, taking derivative in the MDE with respect to $\hat{\rho}$, and using the finite differences method over $N+1$ nodes between $\hat{\rho} = 0$ and $\hat{\rho} = 1$ (see appendix A for a detailed derivation of this model), (14) and (17) provide the system's state-equation,

$$\frac{\mathrm{d}}{\mathrm{d}t} \begin{bmatrix} W \\ \hat{\theta} \end{bmatrix} = \begin{bmatrix} F(W, I_p, P_{\text{NBI},i}, P_{\text{EC}}) \\ G(\hat{\theta}, I_p) u(I_p, P_{\text{NBI},i}, P_{\text{EC}}) \end{bmatrix} + \begin{bmatrix} \delta_W \\ \hat{\delta}_{\theta} \end{bmatrix}, \tag{19}$$

where $\hat{\theta} = [\theta_1, \ldots, \theta_m, \ldots, \theta_{N-1}]^T$ is the vector of θ values at the interior discretization nodes, $\theta_m = \theta(\hat{\rho}_m)$, $\hat{\rho}_m = (m-1)\Delta\hat{\rho}$ $(m = 2, \ldots, N)$, $\Delta\hat{\rho} \triangleq 1/N$ is the step employed in the finite differences discretization, $\hat{\delta}_{\theta} = [\delta_{\theta}(\hat{\rho}_1), \ldots, \delta_{\theta}(\hat{\rho}_{N-1})]^T$, where $\delta_{\theta} \triangleq \partial \delta_{\psi} / \partial \hat{\rho}$, $F \triangleq -W/\tau_E^{\text{nom}} + P_{\text{tot}}$, $u = [u_{\eta}, u_{\text{NBI},1}, \ldots, u_{\text{NBI},N_{\text{NBI}}}, u_{\text{EC}} u_{\text{BS}}]^T$ is the virtual input vector, which is a function of the physical inputs to the system I_p, $P_{\text{NBI},i}$, P_{EC}, and $\bar{n}_e$,

$$u_{\eta} = I_p^{-3\gamma/2} P_{\text{tot}}^{-3\epsilon/2} \bar{n}_e^{-3\zeta/2}, \tag{20}$$

$$u_{\text{NBI},i} = I_p^{\gamma(\lambda_{\text{NBI}} - \frac{3}{2})} P_{\text{tot}}^{\epsilon(\lambda_{\text{NBI}} - \frac{3}{2})} \bar{n}_e^{\zeta(\lambda_{\text{NBI}} - \frac{3}{2}) - 1} P_{\text{NBI},i}, \tag{21}$$

$$u_{\text{EC}} = I_p^{\gamma(\lambda_{\text{EC}} - \frac{3}{2})} P_{\text{tot}}^{\epsilon(\lambda_{\text{EC}} - \frac{3}{2})} \bar{n}_e^{\zeta(\lambda_{\text{EC}} - \frac{3}{2}) - 1} P_{\text{EC}}, \tag{22}$$

$$u_{\text{BS}} = I_p^{-\gamma/2} P_{\text{tot}}^{-\epsilon/2} \bar{n}_e^{1 - \zeta/2}, \tag{23}$$

and $G \in \mathbb{R}^{(N-1) \times (N_{\text{NBI}} + 3)}$ is a matrix whose structure is explained next. First, for convenience, G can be written in terms of three components, i.e.,

$$G(\hat{\theta}, I_p) = [G_{\eta}(\hat{\theta}, I_p), G_{\text{aux}}, G_{\text{BS}}(\hat{\theta}, I_p)], \tag{24}$$

where $G_{\eta} \in \mathbb{R}^{(N-1) \times 1}$ is the component associated with u_{η}, and is given by

$$G_{\eta}(\hat{\theta}, I_p) = \begin{bmatrix} \gamma_1 \theta_1 + \beta_1 \theta_2 \\ \alpha_2 \theta_1 + \gamma_2 \theta_2 + \beta_2 \theta_3 \\ \vdots \\ \alpha_{N-2} \theta_{N-3} + \gamma_{N-2} \theta_{N-2} + \beta_{N-2} \theta_{N-1} \\ \alpha_{N-1} \theta_{N-2} + \gamma_{N-1} \theta_{N-1} - \beta_{N-1} k_{I_p} I_p \end{bmatrix}, \tag{25}$$

where $\gamma_{(\cdot)}$, $\beta_{(\cdot)}$ and $\alpha_{(\cdot)}$ are constants that depend on the model parameters and profiles (see appendix A, equations (A.7)–(A.9) and (A.26)), $G_{\text{aux}} \in \mathbb{R}^{(N-1) \times N_{\text{aux}}}$ is a constant component associated with $u_{\text{NBI},i}$ and u_{EC}, and is given by

$$G_{\text{aux}} = \begin{bmatrix} h_{\text{NBI},1}^1 & \cdots & h_{\text{NBI},N_{\text{NBI}}}^1 & h_{\text{EC}}^1 \\ h_{\text{NBI},1}^2 & \cdots & h_{\text{NBI},N_{\text{NBI}}}^2 & h_{\text{EC}}^2 \\ \vdots & \ddots & \vdots & \vdots \\ h_{\text{NBI},1}^{N-2} & \cdots & h_{\text{NBI},N_{\text{NBI}}}^{N-2} & h_{\text{EC}}^{N-2} \\ h_{\text{NBI},1}^{N-1} & \cdots & h_{\text{NBI},N_{\text{NBI}}}^{N-1} & h_{\text{EC}}^{N-1} \end{bmatrix} \tag{26}$$

where $h^{(\cdot)}_{\mathrm{NBI},i}$ and $h^{(\cdot)}_{\mathrm{EC}}$ are constant parameters that depend on the deposition profiles associated with the $N_{\mathrm{aux}} \triangleq N_{\mathrm{NBI}} + 1$ auxiliary sources (see appendix A, equations (A.16) and (A.27)), and $G_{\mathrm{BS}} \in \mathbb{R}^{(N-1)\times 1}$ is the component associated with u_{BS}, and is given by

$$G_{\mathrm{BS}}(\hat{\theta}, I_{\mathrm{p}}) = \begin{bmatrix} \frac{h^1_{\mathrm{BS},1}}{\theta_1} - \frac{h^1_{\mathrm{BS},2}}{\theta_1^2}\frac{\theta_2}{2\Delta\hat{\rho}} \\ \frac{h^2_{\mathrm{BS},1}}{\theta_2} - \frac{h^2_{\mathrm{BS},2}}{\theta_2^2}\frac{\theta_3 - \theta_1}{2\Delta\hat{\rho}} \\ \vdots \\ \frac{h^{N-2}_{\mathrm{BS},1}}{\theta_{N-2}} - \frac{h^{N-2}_{\mathrm{BS},2}}{\theta_{N-2}^2}\frac{\theta_{N-1} - \theta_{N-3}}{2\Delta\hat{\rho}} \\ \frac{h^{N-1}_{\mathrm{BS},1}}{\theta_{N-1}} - \frac{h^{N-1}_{\mathrm{BS},2}}{\theta_{N-1}^2}\frac{-k_{I_{\mathrm{p}}} I_{\mathrm{p}} - \theta_{N-2}}{2\Delta\hat{\rho}} \end{bmatrix} \tag{27}$$

where $h_{\mathrm{BS},(\cdot)}$ are constant parameters that depend on the model profiles and parameters related to the bootstrap current term (see appendix A, equations (A.20) and (A.27)).

For mathematical simplicity during the control synthesis, the variables θ and W are employed instead of the related variables q and β_N, respectively. The relationship between θ and q is given by (1) together with the definition of $\theta \triangleq \partial\psi/\partial\hat{\rho}$, whereas the relationship between W and β_N is given by

$$\beta_N \triangleq \beta_t[\%]\frac{aB_{\phi,0}}{I_{\mathrm{p}}}, \quad \beta_t = \frac{\frac{2}{3}W/V}{B^2_{\phi,0}/(2\mu_0)}, \tag{28}$$

where V is the plasma volume.

The controllable inputs are I_{p}, $P_{\mathrm{NBI},i}$, and P_{EC}, whereas $\bar{n}_{\mathrm{e}}$ is considered as a non-controllable input to the system. Control by means of $\bar{n}_{\mathrm{e}}$ is left out of the scheme because accurate density control in tokamaks can be a really challenging problem, and it would overestimate the real actuation capability existing for current-profile control.

Finally, the boundary condition (3) at $\hat{\rho} = 1$ determines the evolution of q at the edge, q_{edge}, as given by

$$\theta_N = -k_{I_{\mathrm{p}}} I_{\mathrm{p}}, \quad q_{\mathrm{edge}} = -\frac{B_{\phi,0}\rho_b^2}{\theta_N}, \tag{29}$$

where $\theta_N \triangleq \theta(\hat{\rho} = 1)$.

3. Control synthesis

3.1. Boundary control (q_{edge} control) by means of I_{p} modulation

The first step in the control design is to synthesize a control law for I_{p} in order to regulate q_{edge} around a desired target, $q^{\mathrm{tar}}_{\mathrm{edge}}$, or equivalently, to regulate θ_N around a desired value $\theta^{\mathrm{tar}}_N = -B_{\phi,0}\rho_b^2/q^{\mathrm{tar}}_{\mathrm{edge}}$. If I_{p} is taken as

$$\begin{aligned} I_{\mathrm{p}} &= -\frac{\theta^{\mathrm{tar}}_N}{k^*_{I_{\mathrm{p}}}} + K_q \int_{t_0}^{t} \left(\theta_N - \theta^{\mathrm{tar}}_N\right) \mathrm{d}t \\ &= \frac{B_{\phi,0}\rho_b^2}{k_{I_{\mathrm{p}}} q^{\mathrm{tar}}_{\mathrm{edge}}} + K_q \int_{t_0}^{t} \left(\theta_N - \theta^{\mathrm{tar}}_N\right) \mathrm{d}t, \end{aligned} \tag{30}$$

where $k^*_{I_{\mathrm{p}}}$ is the estimate for $k_{I_{\mathrm{p}}}$ previously introduced, $K_q > 0$ is a design parameter, and t_0 is the initial time, then θ_N in (29) can be rewritten as

$$\theta_N = \frac{k_{I_{\mathrm{p}}}}{k^*_{I_{\mathrm{p}}}}\theta^{\mathrm{tar}}_N - k_{I_{\mathrm{p}}} K_q \int_{t_0}^{t} \left(\theta_N - \theta^{\mathrm{tar}}_N\right) \mathrm{d}t. \tag{31}$$

Re-arranging terms in equation (31), and defining $\tilde{\theta}_N \triangleq \theta_N - \theta^{\mathrm{tar}}_N$, it is found that

$$\tilde{\theta}_N = \frac{k_{I_{\mathrm{p}}} - k^*_{I_{\mathrm{p}}}}{k^*_{I_{\mathrm{p}}}}\theta^{\mathrm{tar}}_N - k_{I_{\mathrm{p}}} K_q \int_{t_0}^{t} \tilde{\theta}_N \, \mathrm{d}t. \tag{32}$$

and taking time derivative, (32) becomes

$$\frac{\mathrm{d}\tilde{\theta}_N}{\mathrm{d}t} = \frac{k_{I_{\mathrm{p}}} - k^*_{I_{\mathrm{p}}}}{k^*_{I_{\mathrm{p}}}}\frac{\mathrm{d}\theta^{\mathrm{tar}}_N}{\mathrm{d}t} - k_{I_{\mathrm{p}}} K_q \tilde{\theta}_N - \frac{\mathrm{d}k_{I_{\mathrm{p}}}}{\mathrm{d}t} K_q \int_{t_0}^{t} \tilde{\theta}_N \, \mathrm{d}t. \tag{33}$$

In the case of constant or slowly varying θ^{tar}_N and $k_{I_{\mathrm{p}}}$ (i.e., the plasma equilibrium changes slowly, so R_0, $\hat{G}$, and $\hat{H}$, and thus $k_{I_{\mathrm{p}}}$, vary slowly), equation (33) becomes,

$$\frac{\mathrm{d}\tilde{\theta}_N}{\mathrm{d}t} = -k_{I_{\mathrm{p}}} K_q \tilde{\theta}_N, \tag{34}$$

which is an asymptotically stable system with, for example, a Lyapunov function $V = \frac{1}{2}\tilde{\theta}^2_N$ (for a definition of asymptotical stability and its proof via Lyapunov theory, see appendix B, equations (B.5) through (B.9)). It can be noted that the assumptions of constant or slowly varying θ^{tar}_N and $k_{I_{\mathrm{p}}}$ are often well satisfied at some point of the tokamak-plasma discharge, specially at the flat-top phase and/or in steady-state conditions. More importantly, even when these conditions are not satisfied, the control law (30) guarantees tracking of θ^{tar}_N, although with a non-zero tracking error.

3.2. Diffusion control (W control) by means of P_{tot} modulation

The second step in the control design is to synthesize a control law for P_{tot} in order to regulate W around a desired target, W^{tar}, or equivalently, to regulate β_N around a desired target $\beta^{\mathrm{tar}}_N \triangleq \frac{\frac{4}{3}\mu_0 W^{\mathrm{tar}} a}{B_{\phi,0} I_{\mathrm{p}} V}$. This control law for P_{tot} is composed of two contributions: a nominal component, $P^{\mathrm{nom}}_{\mathrm{tot}}$ (derived in section 3.2.1), and a robust component, $P^{\mathrm{rob}}_{\mathrm{tot}}$ (derived in section 3.2.2), i.e., $P_{\mathrm{tot}} = P^{\mathrm{nom}}_{\mathrm{tot}} + P^{\mathrm{rob}}_{\mathrm{tot}}$.

3.2.1. Nominal W control via Lyapunov theory. First, the nominal W-subsystem ($\delta_W = 0$) is considered, i.e.,

$$\frac{\mathrm{d}W}{\mathrm{d}t} = -\frac{W}{\tau^{\mathrm{nom}}_{\mathrm{E}}} + P_{\mathrm{tot}}, \tag{35}$$

which, using the deviation variable $\tilde{W} \triangleq W - W^{\mathrm{tar}}$, can be rewritten as

$$\frac{\mathrm{d}\tilde{W}}{\mathrm{d}t} = -\frac{W}{\tau^{\mathrm{nom}}_{\mathrm{E}}} + P^{\mathrm{nom}}_{\mathrm{tot}} - \frac{\mathrm{d}W^{\mathrm{tar}}}{\mathrm{d}t}. \tag{36}$$

If the right-hand side of (36) is set as

$$-\frac{W}{\tau_{\mathrm{E}}^{\mathrm{nom}}}+P_{\mathrm{tot}}^{\mathrm{nom}}=-K_{\mathrm{E}}\tilde{W}+\frac{\mathrm{d}W^{\mathrm{tar}}}{\mathrm{d}t}, \tag{37}$$

where $K_{\mathrm{E}}>0$ is a design parameter, then (36) is reduced to $\mathrm{d}\tilde{W}/\mathrm{d}t=-K_{\mathrm{E}}\tilde{W}$, which ensures asymptotical stability of the nominal W-subsystem with, for example, a Lyapunov function $V_W=\frac{1}{2}\tilde{W}^2$ (for a definition of asymptotical stability and its proof via Lyapunov theory, see appendix B, equations (B.5) through (B.9)). Because I_{p} is determined by the control law (30) and $\bar{n}_{\mathrm{e}}$ is assumed to be a non-controllable input, $P_{\mathrm{tot}}^{\mathrm{nom}}$ is the only variable that needs to be determined within the nominal energy confinement time, $\tau_{\mathrm{E}}^{\mathrm{nom}}$. Thus, the nonlinear equation (37) allows for computing the value of $P_{\mathrm{tot}}^{\mathrm{nom}}$ that stabilizes the nominal W-subsystem.

3.2.2. Robust W control via Lyapunov redesign. In the presence of the uncertainty δ_W, the extra term $P_{\mathrm{tot}}^{\mathrm{rob}}$ is added so that $P_{\mathrm{tot}}=P_{\mathrm{tot}}^{\mathrm{nom}}+P_{\mathrm{tot}}^{\mathrm{rob}}$ makes the W-subsystem robustly stable. The extra term $P_{\mathrm{tot}}^{\mathrm{rob}}$ is designed using Lyapunov redesign techniques. The derivation in this section follows the same steps as those shown in appendix C. If $P_{\mathrm{tot}}^{\mathrm{rob}}$ is taken as

$$P_{\mathrm{tot}}^{\mathrm{rob}}=-\delta_W^{\max}\frac{\tilde{W}}{|\tilde{W}|}, \tag{38}$$

where $\delta_W^{\max}>0$ is the maximum attainable δ_W (i.e., $|\delta_W|\leqslant\delta_W^{\max}$), the W-subsystem dynamics in (19) can be written as

$$\frac{\mathrm{d}\tilde{W}}{\mathrm{d}t}=-\frac{W}{\tau_{\mathrm{E}}^{\mathrm{nom}}}+P_{\mathrm{tot}}-\frac{\mathrm{d}W^{\mathrm{tar}}}{\mathrm{d}t}+\delta_W=-K_{\mathrm{E}}\tilde{W}+P_{\mathrm{tot}}^{\mathrm{rob}}+\delta_W, \tag{39}$$

where the definition $\tilde{W}\triangleq W-\bar{W}$ and (37) have been employed. Using the Lyapunov function $V_W=\frac{1}{2}\tilde{W}^2$, it is found that

$$\begin{aligned}\dot{V}_W&=-K_{\mathrm{E}}\tilde{W}^2-\delta_W^{\max}\frac{\tilde{W}^2}{|\tilde{W}|}+\delta_W\tilde{W}\\&\leqslant-K_{\mathrm{E}}\tilde{W}^2-\delta_W^{\max}|\tilde{W}|+\delta_W^{\max}|\tilde{W}|=-K_{\mathrm{E}}\tilde{W}^2,\end{aligned} \tag{40}$$

so the W-subsystem dynamics remains asymptotically stable even in the presence of δ_W. However, the robust control law (38) needs to be modified to avoid division by zero when $|W|\to 0$. First, a design parameter $\epsilon>0$ is defined. When $|W|\geqslant\epsilon/\delta_W^{\max}$, the singularity in the control law (38) is not an issue because $\epsilon>0$ by design, so $|W|>0$ as well. On the other hand, when $|W|<\epsilon/\delta_W^{\max}$, if $P_{\mathrm{tot}}^{\mathrm{rob}}$ is taken as

$$P_{\mathrm{tot}}^{\mathrm{rob}}=-(\delta_W^{\max})^2\frac{\tilde{W}}{\epsilon}, \tag{41}$$

then the time derivative of V_W becomes

$$\begin{aligned}\dot{V}_W&=-K_{\mathrm{E}}\tilde{W}^2-\left(\delta_W^{\max}\right)^2\frac{\tilde{W}^2}{\epsilon}+\delta_W\tilde{W}\\&\leqslant-K_{\mathrm{E}}\tilde{W}^2-\left(\delta_W^{\max}\right)^2\frac{\tilde{W}^2}{\epsilon}+\delta_W^{\max}|\tilde{W}|\\&\leqslant-K_{\mathrm{E}}\tilde{W}^2+\frac{\epsilon}{4},\end{aligned} \tag{42}$$

where the term $g\triangleq-\left(\delta_W^{\max}\right)^2\frac{\tilde{W}^2}{\epsilon}+\delta_W^{\max}|\tilde{W}|$ has been bounded by $\epsilon/4$ because it has a maximum at $\delta_W^{\max}|\tilde{W}|=\epsilon/2$. The bound to $\dot{V}_W$ found in (42) actually applies to $\dot{V}_W$ in the region $|W|\geqslant\epsilon/\delta_W^{\max}$ as well, so it fulfills the conditions in (B.10) and (B.11) with $\mu<\epsilon/(4K_{\mathrm{E}})$, and $\tilde{W}$ is in fact bounded as stated in (B.12) and (B.13) (see appendix B). Therefore, it can be concluded that the control law

$$P_{\mathrm{tot}}^{\mathrm{rob}}=-\delta_W^{\max}\frac{\tilde{W}}{|\tilde{W}|},\quad\text{if }\delta_W^{\max}|W|\geqslant\epsilon, \tag{43}$$

$$P_{\mathrm{tot}}^{\mathrm{rob}}=-(\delta_W^{\max})^2\frac{\tilde{W}}{\epsilon},\quad\text{if }\delta_W^{\max}|W|<\epsilon, \tag{44}$$

ensures $|\tilde{W}|\leqslant\epsilon/(4K_{\mathrm{E}})$ after some finite time, so it is necessary to set $\epsilon\to 0$ in order to have a bound that is tight enough.

3.3. Interior q-profile control by means of $P_{\mathrm{NBI},i}$ and P_{EC} modulation

3.3.1. Analysis of the nominal dynamics for feedback linearization. In this section, the nominal $\hat{\theta}$-subsystem ($\hat{\delta}_\theta=0$) is studied in order to determine if a FB-linearization control law for the interior nodes of the q profile can be found together with the I_{p} control law (30) for q_{edge} control and the P_{tot} control laws (37), (43) and (44) for β_N control. Through FB linearization [17], a change of variables $z=T(\hat{\theta})$ and/or a control law $u=r(\hat{\theta},v)$ are sought so that the nominal $\hat{\theta}$-dynamics in (19) can be rewritten as a linear system, i.e., so that the dynamical equation

$$\begin{aligned}\frac{\mathrm{d}\hat{\theta}}{\mathrm{d}t}&=G(\hat{\theta},I_{\mathrm{p}})u\\&=G_\eta u_\eta+G_{\mathrm{aux}}[u_{\mathrm{NBI},1},\ldots,u_{\mathrm{NBI},N_{\mathrm{NBI}}},u_{\mathrm{EC}}]^T\\&\quad+G_{\mathrm{BS}}u_{\mathrm{BS}},\end{aligned} \tag{45}$$

can be rewritten as

$$\frac{\mathrm{d}z}{\mathrm{d}t}=Az+Bv, \tag{46}$$

for some constant matrices A and B, and an input vector v.

First, the deviation variable $\tilde{\theta}$ can be defined as $\tilde{\theta}\triangleq\hat{\theta}-\hat{\theta}^{\mathrm{tar}}$, where $\hat{\theta}^{\mathrm{tar}}$ is the desired target for $\hat{\theta}$. Equation (45) can be rewritten as

$$\begin{aligned}\frac{\mathrm{d}\tilde{\theta}}{\mathrm{d}t}&=Gu-\frac{\mathrm{d}\hat{\theta}^{\mathrm{tar}}}{\mathrm{d}t}\\&=G_\eta u_\eta+G_{\mathrm{aux}}[u_{\mathrm{NBI},1},\ldots,u_{\mathrm{NBI},N_{\mathrm{NBI}}},u_{\mathrm{EC}}]^T\\&\quad+G_{\mathrm{BS}}u_{\mathrm{BS}}-\frac{\mathrm{d}\hat{\theta}^{\mathrm{tar}}}{\mathrm{d}t}.\end{aligned} \tag{47}$$

By inspection, it can be noted that if $z=\tilde{\theta}$, and the right-hand side of (47) is set as

$$\begin{aligned}&G_\eta u_\eta+G_{\mathrm{aux}}[u_{\mathrm{NBI},1},\ldots,u_{\mathrm{NBI},N_{\mathrm{NBI}}},u_{\mathrm{EC}}]^T\\&\quad+G_{\mathrm{BS}}u_{\mathrm{BS}}-\frac{\mathrm{d}\hat{\theta}^{\mathrm{tar}}}{\mathrm{d}t}=A\tilde{\theta}+Bv,\end{aligned} \tag{48}$$

then the nominal θ-subsystem (45) is in fact linearized by FB. The key is to see whether G (or its components G_η, G_{aux}, and G_{BS}) actually allows for obtaining $u = r(\hat{\theta}, v)$ by solving (48).

It can be seen that G_η and G_{BS} do not play a role for FB linearization purposes. Under $q_{\text{edge}} + \beta_N$ FB, I_{p} is determined by (30), P_{tot} is determined by (37) together with (43) and (44), and $\bar{n}_{\text{e}}$ is assumed as a non-controllable variable in this work. Therefore, u_η and u_{BS} in (20) and (23) are also determined by the $q_{\text{edge}} + \beta_N$ FB control laws. The only virtual inputs available for interior q-profile control are $u_{\text{NBI},1}, \ldots, u_{\text{NBI},N_{\text{NBI}}}, u_{\text{EC}}$. It must also be noted that $u_{\text{NBI},1}, \ldots, u_{\text{NBI},N_{\text{NBI}}}, u_{\text{EC}}$ are not independent due to the constraint imposed by the P_{tot} control law (37), (43) and (44) (see the definition of P_{tot} in (11)). Rearranging terms and embedding (11) within the FB linearization scheme, (48) can be rewritten as

$$\begin{bmatrix} G^*_{\text{aux}} \\ 1 \ldots 1 \end{bmatrix} [P_{\text{NBI},1}, \ldots, P_{\text{NBI},N_{\text{NBI}}}, P_{\text{EC}}]^T = \begin{bmatrix} A\tilde{\theta} + Bv + \dfrac{\mathrm{d}\tilde{\theta}^{\text{tar}}}{\mathrm{d}t} - (G_\eta u_\eta + G_{\text{BS}} u_{\text{BS}}) \\ P_{\text{tot}} \end{bmatrix}, \quad (49)$$

where $G^*_{\text{aux}}[P_{\text{NBI},1}, \ldots, P_{\text{NBI},N_{\text{NBI}}}, P_{\text{EC}}]^T = G_{\text{aux}}[u_{\text{NBI},1}, \ldots, u_{\text{NBI},N_{\text{NBI}}}, u_{\text{EC}}]^T$ (see the definition of the virtual inputs $u_{(\cdot)}$, equations (20)–(23)), and P_{tot} is the value obtained from (37) together with (43) and (44). The following matrix

$$G^* = \begin{bmatrix} G^*_{\text{aux}} \\ 1 \ldots 1 \end{bmatrix} \in \mathbb{R}^{N \times N_{\text{aux}}}, \quad (50)$$

defines whether $u = r(\hat{\theta}, v)$ can actually be obtained from the linear system (49). In other words, for (49) to effectively achieve the FB linearization of (45), there must exist at least one solution for $P_{\text{NBI},1}, \ldots, P_{\text{NBI},N_{\text{NBI}}}, P_{\text{EC}}$. This, in general, can only be ensured if G^* is a full row-rank matrix, i.e., if G^* spans $\mathbb{R}^N$, which in turn requires that $N_{\text{aux}} \geqslant N$. If G^* is not full row rank, a solution of (49) is possible only in the case that the right-hand side of the equation lies within the subspace spanned by G^*, i.e., only for particular values of $\hat{\theta}^{\text{tar}}$, I_{p}, and P_{tot} (which define the right-hand side of (49)). Therefore, if G^* is not full row rank, only 'approximate' (e.g., in a least-squares sense) FB linearization of the system can be guaranteed in general (see, for example, our previous work [19]). On the other hand, having $N_{\text{aux}} > N$ would imply that an extra number of $N_{\text{aux}} - N$ interior nodes could be controlled independently as long as physical saturation limits are not reached. Because it seems reasonable to control as many points of the current profile as possible, the finite-differences discretization is carried out with $N = N_{\text{aux}}$, yielding a square G^* matrix. This results in (49) being a square, linear system with N_{aux} unknowns and equations, which has a unique solution as long as G^* is full rank.

It can be noted that, in order to fulfill the full rank condition when G^* is square, its structure requires that the deposition profiles $j^{(\cdot),i}_{\text{dep}}$ ($(\cdot) = $ NBI, EC) produce linearly independent columns (this idea was first considered for DIII-D in [20], but using the whole matrix G). If that is not the case, then the approach presented in this work is only practical if the NBI/EC sources are 'grouped' so that their deposition profiles compose a linearly independent set of vectors. In the particular case in which all the auxiliary sources have the same deposition profile, then only one group exists. Such case would correspond to having just one controllable input (the total power, P_{tot}), thus it would not be possible to combine interior q-profile control with q_{edge} and β_N control. This would not be an issue of the FB-linearization control approach, but just a lack of actuation capability for interior q-profile control within a given tokamak.

A few interesting conclusions can be drawn from the FB-linearization analysis presented in this section. The first conclusion is that the number of controllable nodes for q-profile control + β_N control is not only limited by the number of available auxiliary sources whose power can be controlled individually, but also by the shape of the deposition profiles of such sources. If $\beta_N + q_{\text{edge}}$ are controlled by P_{tot} and I_{p} but the auxiliary sources do not have different deposition profiles, the model employed for control synthesis tells us that it is not possible to directly control the q profile at any interior node. Both I_{p} and P_{tot} would univocally determine the current diffusion rate by means of the plasma resistivity η, as well as the non-inductive current contribution, j_{ni}, and therefore $\beta_N + q_{\text{edge}}$ control could not be carried out independently of interior q-profile control (see, for example, [5]). Even if q_{edge} is not directly controlled and I_{p} is used for interior q-profile control instead, the effect of I_{p} on the interior q profile would be limited by diffusion. Moreover, I_{p} modulation may be limited by technological constraints (such as the current through the poloidal coils) and physics constraints (e.g., disruptions and/or MHD instabilities), so it may not be suitable to control q at the core.

A second conclusion is that G^* is in fact the tensor relating the subspace of auxiliary power signals, $P_{(\cdot),i}$ ($(\cdot) = $ NBI, EC), and the $\mathrm{d}\hat{\theta}/\mathrm{d}t$ subspace. This is an interesting interpretation, as studying G^* in terms of its singular values indicates the input directions in which q-profile control can be carried out most efficiently, the output directions in which the q profile is more easily controllable, and the maximum/minimum achievable time-derivative for $\hat{\theta}$. Also, the image of the linear transformation $G^* : P_{(\cdot)} \to \dot{\hat{\theta}}$ subject to physical actuator constraints determines the reachable set of θ profiles (and therefore, q profiles) for given q_{edge} and β_N values. Such tool may be of significant interest for tokamak-scenario planning and development.

3.3.2. Nominal q-profile control via state-feedback. As demonstrated in the previous section, the control law (49) reduces the nominal θ-subsystem ($\delta_\theta = 0$) to equation (46) with $z = \tilde{\theta}$ assuming a square, full rank G^* matrix. For example, using a state-FB control law[1] given by

$$v = v_{\text{nom}} = -K\tilde{\theta}, \quad (51)$$

[1] This is just one of many control techniques that could be applied to the feedback-linearized model. State-feedback control is chosen in this work because of its relative theoretical and practical simplicity.

where $K \in \mathbb{R}^{(N-1)\times(N-1)}$ is a design matrix, (46) is reduced to

$$\dot{\tilde{\theta}} = (A - BK)\tilde{\theta}. \tag{52}$$

Exploiting the fact that $B \in \mathbb{R}^{(N-1)\times(N-1)}$, it is possible to set $A = \mathcal{O}$ and $B = \mathcal{I}$ ($\mathcal{O}$ and $\mathcal{I}$ are the zero and identity matrices, respectively, of dimension $\mathbb{R}^{(N-1)\times(N-1)}$) without loss of generality in order to guarantee controllability. In this case it is always possible to find a matrix K to arbitrarily place the eigenvalues of the closed-loop matrix $A - BK$ and stabilize the $\tilde{\theta}$ evolution. It must be taken into account that, although (49) always has a solution for $P_{(\cdot)}$, it may not be within the feasible set due to physical actuation limits. A careful control design of the matrix K together with a reasonable choice of $\hat{\theta}^{\text{tar}}$ must be carried out to avoid actuator saturation for too long periods of time, and the poor performance that it may imply.

3.3.3. Robust q-profile control via Lyapunov redesign. In this section, the uncertainty in the θ-subsystem is not zero ($\hat{\delta}_\theta \neq 0$). The control law is modified so that the θ-subsystem is stabilized even in the presence of this uncertainty. This section follows the same steps as those shown in appendix C. Under the control law (49), equation (46) with $z = \tilde{\theta}$ and $\hat{\delta}_\theta \neq 0$ becomes

$$\dot{\tilde{\theta}} = A\tilde{\theta} + Bv + \hat{\delta}_\theta, \tag{53}$$

and taking $A = \mathcal{O}$, $B = \mathcal{I}$ as for the nominal control law,

$$\dot{\tilde{\theta}} = v + \hat{\delta}_\theta. \tag{54}$$

The virtual input v is decomposed as $v = v_{\text{nom}} + v_{\text{rob}}$, where v_{nom} is given by (51), and v_{rob} is taken as

$$v_{\text{rob}} = -\delta_\theta^{\max}\frac{\tilde{\theta}}{\|\tilde{\theta}\|_2}, \tag{55}$$

where $\delta_\theta^{\max} > 0$ is the maximum two-norm attainable by $\hat{\delta}_\theta$, i.e., $\|\hat{\delta}_\theta\|_2 \leqslant \delta_\theta^{\max}$. The use of a Lyapunov function $V_\theta = \frac{1}{2}\tilde{\theta}^T\tilde{\theta}$ yields

$$\dot{V}_\theta = \tilde{\theta}^T(v + \hat{\delta}_\theta) = -\tilde{\theta}^T K\tilde{\theta} - \tilde{\theta}^T\delta_\theta^{\max}\frac{\tilde{\theta}}{\|\tilde{\theta}\|_2} + \tilde{\theta}^T\hat{\delta}_\theta. \tag{56}$$

The stability of the nominal system (52) with $A = \mathcal{O}$, $B = \mathcal{I}$, and $v = v_{\text{nom}}$ given by (51) implies that all eigenvalues of K must be positive. Therefore, the first term on the right-hand side of (56) must fulfill the following inequality,

$$\tilde{\theta}^T K\tilde{\theta} \geqslant K_\theta\|\tilde{\theta}\|_2^2, \tag{57}$$

where $K_\theta > 0$ is the smallest eigenvalue of K. Also, as $\tilde{\theta}^T\hat{\delta}_\theta \leqslant \delta_\theta^{\max}\|\tilde{\theta}\|_2$ and $-\tilde{\theta}^T\delta_\theta^{\max}\frac{\tilde{\theta}}{\|\tilde{\theta}\|_2} = -\delta_\theta^{\max}\|\tilde{\theta}\|_2$, equation (56) can be rewritten as

$$\dot{V}_\theta \leqslant K_\theta\|\tilde{\theta}\|_2^2. \tag{58}$$

Thus, the system remains asymptotically stable despite $\hat{\delta}_\theta \neq 0$. However, as also discussed in section 3.2.2, the robust control law (55) must be slightly modified when $\|\tilde{\theta}\|_2 \to 0$ to avoid division by zero. First, a design parameter $\epsilon^* > 0$ is defined. It can be noted that, when $\|\tilde{\theta}\|_2 \geqslant \epsilon^*/\delta_\theta^{\max}$, the control law (55) is fully defined. When $\|\tilde{\theta}\|_2 < \epsilon^*/\delta_\theta^{\max}$, if the control law (55) is modified as

$$v_{\text{rob}} = -\frac{\left(\delta_\theta^{\max}\right)^2}{\epsilon^*}\tilde{\theta}, \tag{59}$$

then the time derivative of V_θ becomes

$$\dot{V}_\theta = -\tilde{\theta}^T K\tilde{\theta} - \tilde{\theta}^T\left(\delta_\theta^{\max}\right)^2\frac{\tilde{\theta}}{\epsilon^*} + \tilde{\theta}^T\hat{\delta}_\theta \tag{60}$$

$$\leqslant -K_\theta\|\tilde{\theta}\|_2^2 - \frac{\left(\delta_\theta^{\max}\right)^2\|\tilde{\theta}\|_2^2}{\epsilon^*} + \delta_\theta^{\max}\|\tilde{\theta}\|_2$$

$$\leqslant -K_\theta\|\tilde{\theta}\|_2^2 + \frac{\epsilon^*}{4}, \tag{61}$$

where $g^* \triangleq -\frac{\left(\delta_\theta^{\max}\right)^2\|\tilde{\theta}\|_2^2}{\epsilon^*} + \delta_\theta^{\max}\|\tilde{\theta}\|_2$ is bounded by $\epsilon^*/4$ because it has a maximum at $\delta_\theta^{\max}\|\tilde{\theta}\|_2 = \epsilon/2$. The bound found in (61) also applies to $\dot{V}_\theta$ in the region $\|\tilde{\theta}\|_2 \geqslant \epsilon^*/\delta_\theta^{\max}$. Therefore, the conditions in (B.10) and (B.11) are fulfilled with $\mu = \epsilon^*/(4K)$, so $\|\tilde{\theta}\|_2$ is in fact bounded as stated in (B.12) and (B.13) (see appendix B). It can be concluded that a robust control law given by

$$v_{\text{rob}} = -\left(\frac{\delta_\theta^{\max}}{\|\tilde{\theta}\|_2} + K\right)\tilde{\theta}, \quad \text{if } \delta_\theta^{\max}\|\tilde{\theta}\|_2 \geqslant \epsilon^*, \tag{62}$$

$$v_{\text{rob}} = -\left(\frac{\left(\delta_\theta^{\max}\right)^2}{\epsilon^*} + K\right)\tilde{\theta}, \quad \text{if } \delta_\theta^{\max}\|\tilde{\theta}\|_2 < \epsilon^*, \tag{63}$$

ensures $\|\tilde{\theta}\|_2 \leqslant \epsilon^*/(4K_\theta)$ after some finite time, so it is necessary to have $\epsilon^* \to 0$ to have a bound that is a tight as possible.

4. One-dimensional simulation study

4.1. Closed-loop performance assessment based on the COTSIM

The performance of the proposed controller is tested in this section using the COTSIM, a code developed by the Plasma Control Group at Lehigh University. In this simulation study, COTSIM evolves the one-dimensional plasma states by using the MDE (2) with boundary conditions (3), the control-oriented models for η and j_{ni} (4)–(6), and the electron heat-transport equation,

$$\frac{3}{2}\frac{\partial n_e T_e}{\partial t} = \frac{1}{\rho_b^2\hat{H}\hat{\rho}}\left(\frac{\hat{G}\hat{H}^2}{\hat{F}}\chi_e n_e\frac{\partial T_e}{\partial\hat{\rho}}\right) + Q_e, \tag{64}$$

where χ_e is the electron thermal diffusivity, and Q_e is the electron heat deposition from different sources. For χ_e, a mixed, semi-empirical Bohm/Gyro-Bohm model based on dimensional analysis is employed [23],

$$\chi_e = \frac{T_e(\text{eV})}{B_{\phi,0}}F\left(\rho_*, q, \frac{a\nabla p_e}{p_e}, \hat{\rho}, \frac{\mathrm{d}q}{\mathrm{d}\hat{\rho}}, \frac{a\nabla T_e}{T_e}\bigg|_{\hat{\rho}=\hat{\rho}_{\text{TB}}}\right), \tag{65}$$

where F is a non-dimensional function which depends on the normalized gyro-radius, ρ_*, q and its spatial derivative, the

electron pressure, p_e, and its gradient, $\hat{\rho}$, T_e and its gradient, and $\hat{\rho}_{TB}$ is the $\hat{\rho}$-coordinate of the edge transport barrier. It is known that heat transport normally increases at higher pressure gradients, but decreases at higher currents and low to negative magnetic shear, thus χ_e increases with q and ∇p_e, but decreases with $dq/d\hat{\rho}$. It can be noted that both current and heat transport are coupled through χ_e (which is a function of q and its spatial derivative) and η (which is a function of T_e).

As another difference from the model used for control synthesis (section 2), ohmic, radiation, and collision effects are considered in the simulation study. Therefore, the electron heating is modeled as

$$Q_e = Q_{aux} + Q_{Ohm} - Q_{rad} + Q_{collisions}, \tag{66}$$

where Q_{aux} is the heating produced by auxiliary heating methods (NBI, ECH, etc), Q_{Ohm} is the ohmic heating power, Q_{rad} represents the radiation losses, and $Q_{collisions}$ is the energy gain/loss of the electrons due to collisions with ions. In this simulation study, the auxiliary heating is modeled in COTSIM as

$$Q_{aux}(\hat{\rho},t) = \sum_{i=1}^{i=N_{NBI}} Q^{prof}_{NBI,i}(\hat{\rho})P_{NBI,i}(t) + Q^{prof}_{EC}(\hat{\rho})P_{EC}(t), \tag{67}$$

where $Q^{prof}_{(\cdot)}(\hat{\rho})$ is a deposition profile (fixed in time) associated with the corresponding auxiliary source. The ohmic heating, Q_{Ohm}, is modeled as

$$Q_{Ohm}(\hat{\rho},t) = \eta(\hat{\rho},t)j_{tor}(\hat{\rho},t)^2, \tag{68}$$

where $j_{tor}(\hat{\rho},t)$ is the toroidal current density. The radiative losses, Q_{rad}, considered in this study are Bremsstrahlung losses only, which are modeled as

$$Q_{rad}(\hat{\rho},t) = k_{brem}Z_{eff}n_e(\hat{\rho},t)^2\sqrt{T_e(\hat{\rho},t)}, \tag{69}$$

where k_{brem} is the Bremsstrahlung constant. Finally, the collision-associated heating, $Q_{collisions}$, is modeled as

$$Q_{collisions}(\hat{\rho},t) = \nu_e(\hat{\rho},t)n_e(\hat{\rho},t)\left(T_i(\hat{\rho},t) - T_e(\hat{\rho},t)\right), \tag{70}$$

where T_i is the ion temperature, and ν_e is the electron–ion collisionality, given by

$$\nu_e(\hat{\rho},t) = 0.041\frac{n_e(\hat{\rho},t)}{T_e(\hat{\rho},t)^{\frac{3}{2}}A_i}, \tag{71}$$

where A_i is the effective mass of the plasma ions. The total plasma energy, W, is obtained from 1D profiles as

$$W = \frac{3}{2}\int_V (n_eT_e + n_iT_i)dV, \tag{72}$$

where n_i is the ion density. For n_e, a 0.5D model like that in (8) is employed. In addition, n_i and T_i are calculated as $n_i = c_n n_e$, $T_i = c_T T_e$, for some constants c_n and c_T.

It must be noted that, although several simplifying assumptions are still made, the model used for the simulation study definitely represents an increase in complexity with respect to the model employed for control synthesis in section 2. This, therefore, provides an effective testbed to assess the robustness of the controller against model uncertainties. COTSIM provides a fast, reliable, closed-loop simulation platform for assessing the performance of a controller during the iterative control-design process before experimental testing. Due to its modular nature, physics complexity in source and transport models can be added if needed. For instance, a more realistic model for $Q_{aux}(\hat{\rho},t)$ taking into account the influence of n_e or T_e on the auxiliary power deposition could be easily added, a different model for χ_e could be adopted, or different assumptions on the ion density and temperature could be made.

4.2. Simulation studies in DIII-D H-mode scenario

The simulation scenario in these studies corresponds to an AT DIII-D scenario. In particular, the experimental inputs from DIII-D shot 147 634 are employed to run a simulation in COTSIM. Relevant magnitudes during shot 147 634 are shown in figure 1, whereas other relevant machine and plasma parameters are given by $B_T = 1.7$ T, $R_0 = 1.8$ m, $a = 0.6$ m, $\kappa = 1.7$, and $f_{NI} \approx 75\%$ (where f_{NI} is the non-inductive current fraction). More details about this shot can be found, for example, in [24]. In addition, the physical saturation limits considered are $P^{max}_{NBI,ON} = 10$ MW, $P^{max}_{NBI,OFF} = 6$ MW, and $P^{max}_{EC} = 3.5$ MW. Finally, based on experimental data, $c_n = 1$ and $c_T = 2$ are employed in these simulations. This assumption for T_i is different from the one made in section 2 for the control-synthesis model. Moreover, all sources of heating are considered during the simulation studies as stated in (66). This represents another test of the robustness of the controller against unmodeled dynamics in the control-synthesis model.

The evolutions for q and β_N predicted by this simulation using the experimental inputs from shot 147 634 are denoted as q^{exp} and β_N^{exp}, respectively. Both q^{exp} and β_N^{exp} are employed in the three simulation cases presented in this section to define the target evolutions to be tracked by the FB controller. Three groups of auxiliary sources are considered, i.e., $N_{aux} = 3$. Those groups are on-axis NBI's (whose power is denoted by $P_{NBI,ON}$), off-axis NBI's (whose power is denoted by $P_{NBI,OFF}$) and EC. This ensures that G^* is always full rank, and that the FB-linearization control law (49) is always defined. As a result, 2 interior nodes of the q profile are controllable. The controller is configured to control q at the nodes $\hat{\rho} = 0.1$ and $\hat{\rho} = 0.4$, as regulation of the value of q at these nodes may allow for significant shaping of the current profile. However, this choice is arbitrary from an unsaturated controllability perspective as discussed in section 3.3.1 and only pretends to illustrate the capabilities of the controller.

4.2.1. Simulation study 1: reproduction of target shot via feedback control.

The goal of this first simulation study is to test the controller's ability to reproduce a given target shot by correcting through FB the chosen feedforward (FF) actuator trajectories. The targets for q and β_N are chosen in this case simply as $q^{tar} = q^{exp}$ and $\beta_N^{tar} = \beta_N^{exp}$, i.e., the goal is to reproduce the simulated version of DIII-D shot 147 634 via FB regulation. However, in order to demonstrate the nonlinear

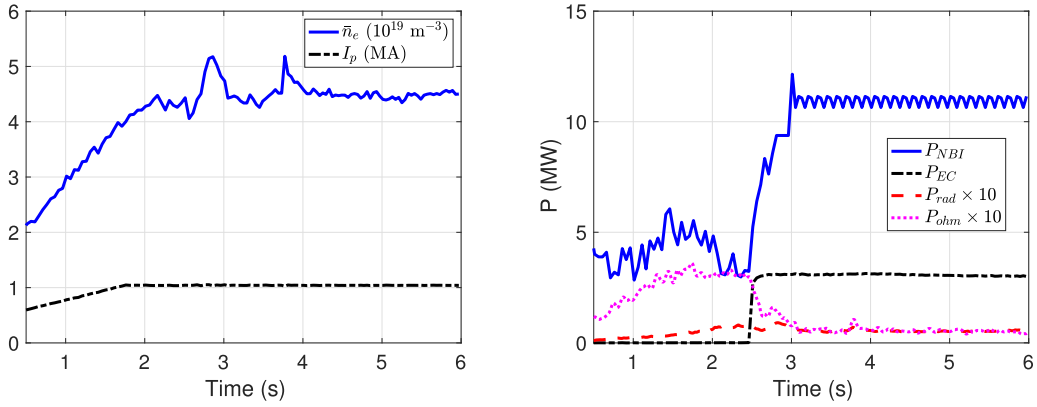

Figure 1. Time evolution of plasma magnitudes during DIII-D shot 147 634: (*a*) line-average electron density, $\bar{n}_\mathrm{e}$, and plasma current, I_p; (*b*) NBI power, P_NBI, EC power, P_EC, radiative power, P_rad, and ohmic power, P_ohm.

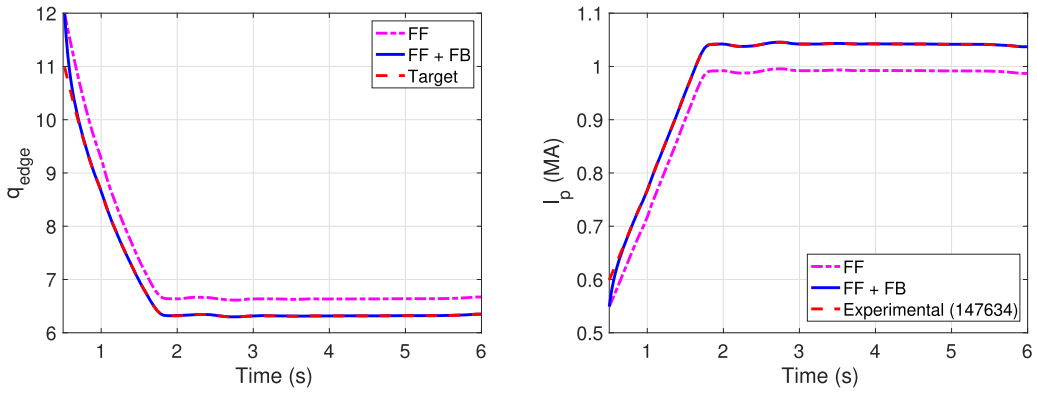

Figure 2. Simulation study 1: time evolutions for q_edge and I_p in FF-only (dashed-dotted magenta) and FF + FB (solid blue) simulations, together with the target $q_\mathrm{edge}^\mathrm{tar}$ and the experimental I_p from shot 147 634 (dashed red). The FB controller modifies I_p in order to achieve the value of q_edge obtained with the experimental inputs from shot 147 634.

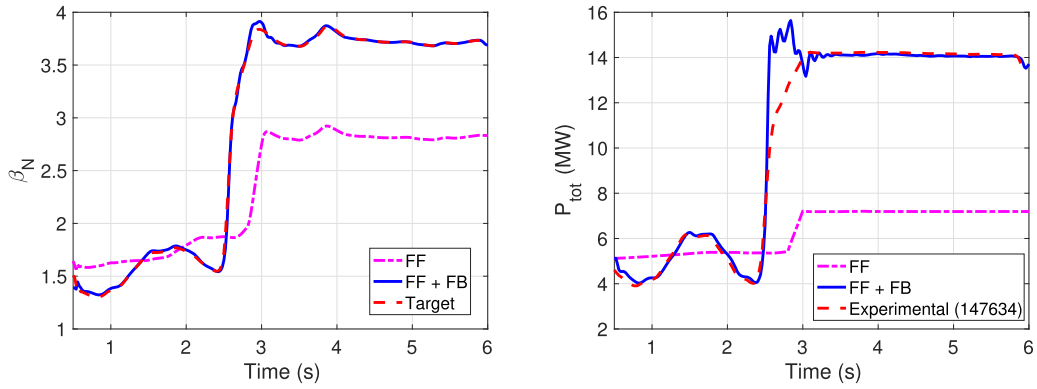

Figure 3. Simulation study 1: time evolutions for β_N and P_tot in FF-only (dashed-dotted magenta) and FF + FB (solid blue) simulations, together with the target β_N^tar and the experimental P_tot from shot 147 634 (dashed red). The FB controller modulates P_tot in order to achieve a β_N evolution in FF + FB that matches the β_N evolution obtained with the experimental inputs from shot 147 634, β_N^exp.

FB controller's capabilities, the FF inputs must be chosen differently from the experimental inputs from shot 147 634 used to predict q^exp and β_N^exp. Therefore, in this simulation study the FF actuator trajectories are defined as follows: I_p is taken from shot 147 634 but decreased by 0.05 MA, $\bar{n}_\mathrm{e}$ is adopted as in shot 147 634, both on-axis and off-axis NBI powers are chosen as constants, with $P_\mathrm{NBI,ON} = 4$ MW and $P_\mathrm{NBI,OFF} = 1$ MW, and the EC power is defined as a step function going from $P_\mathrm{EC} = 0$ to $P_\mathrm{EC} = 2$ MW at 3 s. Figures 2–6 compare the abilities of both the FF-only and the FF + FB controllers to track the desired targets. In the latter case, the FB component of the controller, given by the nonlinear robust control law proposed

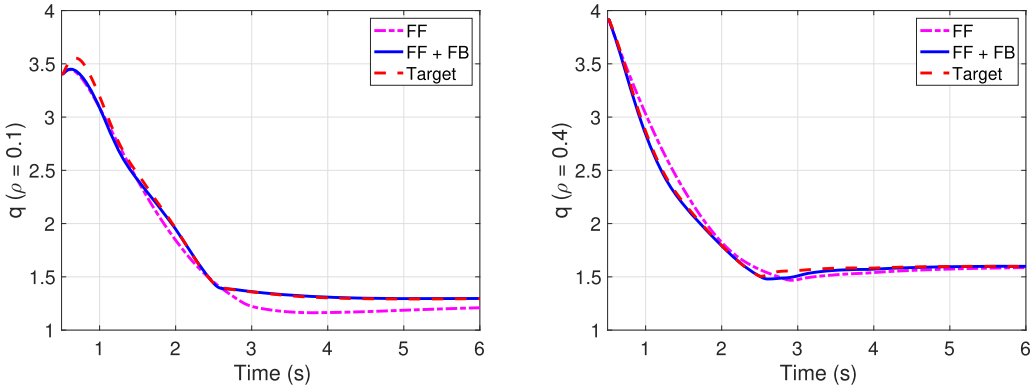

Figure 4. Simulation study 1: time evolutions for q at $\hat{\rho} = 0.10, 0.40$ in FF-only (dashed-dotted magenta) and FF + FB (solid blue) simulations, together with the target q^{tar} (dashed red). Successful q-profile tracking is achieved by the FB controller.

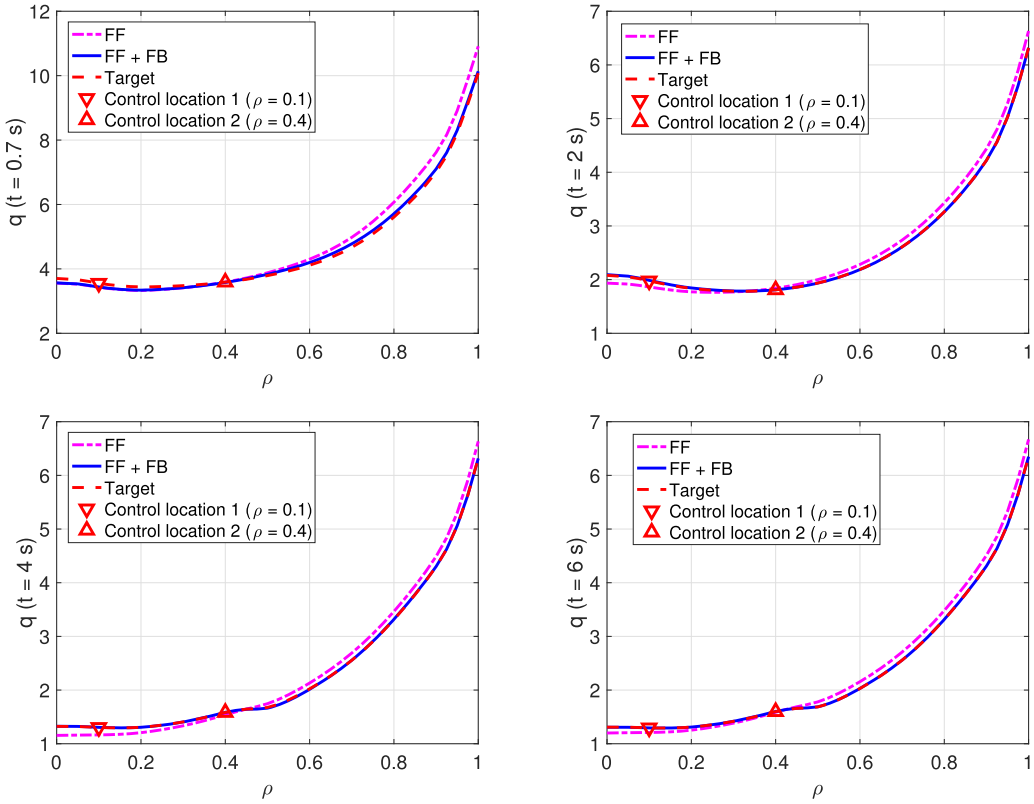

Figure 5. Simulation study 1: comparison of q profiles at $t = 0.7$, 2, 4, and 6 s in FF-only (dashed-dotted magenta) and FF + FB (solid blue) simulations, together with the target q^{tar} (dashed red) and spatial locations for interior q-profile control (red triangles). The q profile is shaped by the FB controller so that it matches the q profile obtained with the experimental inputs from shot 147 634, q^{exp}.

in this work, corrects the FF component to effectively recover the experimental inputs from shot 147 634 and track the target q and β_N. Figure 2 shows the q_{edge} evolutions together with the target $q^{\text{tar}}_{\text{edge}}$, as well as the I_{p} trajectories. Figure 3 shows the β_N evolutions together with the target β^{tar}_N, as well as the P_{tot} trajectories. Figure 4 shows the q-profile evolutions and the corresponding target, q^{tar}, at the two control nodes $\hat{\rho} = 0.1$ and $\hat{\rho} = 0.4$. Figure 5 shows the q profiles at particular instants in time ($t = 0.7$ s, 2 s, 4 s, and 6 s) together with the target q^{tar}. The spatial locations for interior q-profile control are also marked in this figure. Finally, figure 6 shows the NBI and EC power trajectories.

Figure 2 shows that the controller regulates q_{edge} around $q^{\text{tar}}_{\text{edge}}$ in FF + FB, achieving rapid convergence (in about 0.2 s). This is done by increasing I_{p} with respect to its FF value until it reaches the experimental value from shot 147 634. Also, figure 3 shows how β_N is successfully regulated in FF + FB around β^{tar}_N, which is significantly higher than the β_N evolution in FF. This is achieved by modulating P_{tot} until around 2.5 s, and then increasing it substantially. The resulting FF + FB trajectory for P_{tot} is not a superposition of step signals as in the FF case, and instead it follows the trend of the experimental evolution of P_{tot} from the target shot 147 634. It must be emphasized, however, that the controller has no

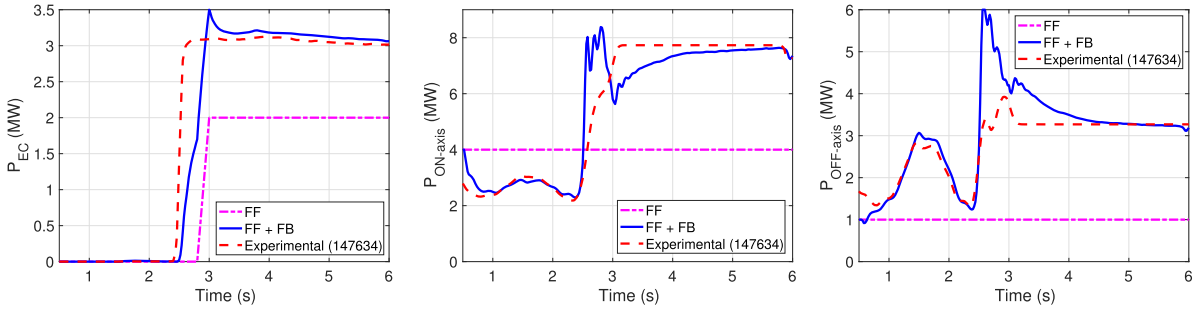

Figure 6. Simulation study 1: time evolution for P_{EC}, $P_{\mathrm{NBI,ON}}$, and $P_{\mathrm{NBI,OFF}}$ in FF-only (dashed-dotted magenta) and FF + FB (solid blue), together with the experimental inputs from shot 147 634 (dashed-red target). In FF + FB, the actuator trajectories calculated by the controller are very close to the experimental trajectories from shot 147 634 despite having no information about them.

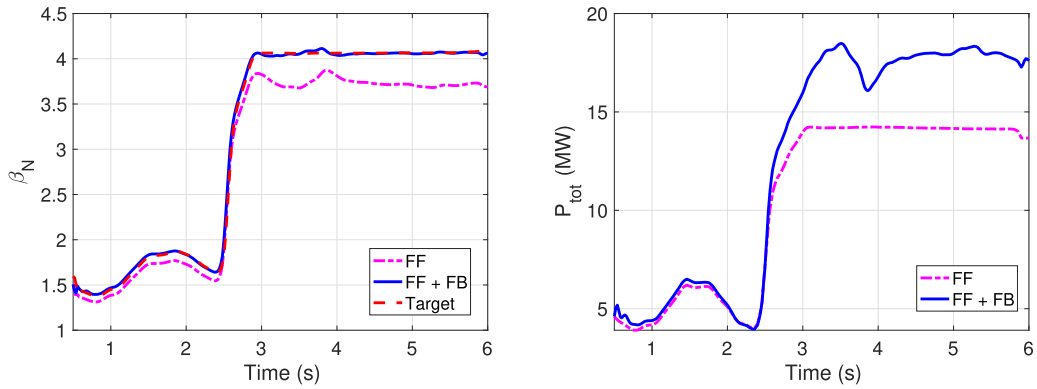

Figure 7. Simulation study 2: time evolutions for β_N and P_{tot} in FF-only (dashed-dotted magenta) and FF + FB (solid blue) simulations, together with the target β_N^{tar} (dashed red). By increasing P_{tot} and shaping the q profile, β_N can be increased and β_N^{tar} can be successfully tracked.

information about the experimental inputs I_{p} and P_{tot} from shot 147 634 (only $q_{\mathrm{edge}}^{\mathrm{tar}}$ and β_N^{tar} are fed into the controller).

Figures 4 and 5 demonstrate the capability of the controller to reproduce the current-profile evolution from shot 147 634. From figure 4, it can be seen that q is properly regulated around q^{tar} in FF + FB at the two control locations $\hat{\rho} = 0.1$ and $\hat{\rho} = 0.4$. Fastest converge of q towards q^{tar} is achieved in FF + FB at $\hat{\rho} = 0.4$, possibly due to the lower T_{e} at such location (which implies a higher η, and therefore, a higher capability to initially modify the q profile), as well as having direct EC current-deposition in such region. Tracking of q at $\hat{\rho} = 0.1$ seems slightly more challenging, particularly in the beginning of the simulation, when it takes around 1 s for q to be driven close to q^{tar}. In any case, successful q-profile regulation is also achieved at $\hat{\rho} = 0.1$ in FF + FB, whereas the FF evolution notably drifts away from q^{tar}. Moreover, target tracking is better at $\hat{\rho} = 0.1$ than at $\hat{\rho} = 0.4$ around $t = 2.5$ s, when the target becomes flat, showing no overshoot. In FF, q remains close to q^{tar} at $\hat{\rho} = 0.4$ as a result of the global q profile shape (see figure 5), but convergence of q towards q^{tar} at the two control locations is not guaranteed in the FF case.

From figure 5, it can be seen that the current profile in FF + FB has a significantly different shape than in the FF case. Whereas q is reduced in FF + FB with respect to the FF evolution in the region $\hat{\rho} \gtrapprox 0.4$, it is increased in the region $\hat{\rho} \lessapprox 0.4$, yielding a substantial change in the q-profile shape. It can also be appreciated that, in this simulation case, controlling q at three spatial locations (i.e., the edge $\hat{\rho} = 1$ together with the two interior locations $\hat{\rho} = 0.1$ and $\hat{\rho} = 0.4$) actually allows for accurately matching the whole target profile. This is a direct consequence of the controllability limits since, in order to control three spatial locations of the q profile together with β_N, all the degrees of freedom in terms of actuation must be exploited. Under these conditions there is one possible control solution to track the targets, which is for the controller to recover the experimental inputs associated with the target shot as shown in the figures. It is therefore not surprising that the whole q profile is recovered as well. Figure 5 shows that the q profile responds more rapidly to boundary control actions (i.e., q_{edge} control by means of I_{p}) than to interior control actions by means of $P_{\mathrm{NBI,ON}}$, $P_{\mathrm{NBI,OFF}}$, and P_{EC}, but both actuation mechanisms are necessary for an efficient regulation of the whole q profile. Figure 6 shows how heavily the controller needs to correct the FF trajectories for $P_{\mathrm{NBI,ON}}$, $P_{\mathrm{NBI,OFF}}$, and P_{EC} in order to track the desired targets for $q(\hat{\rho} = 0.1)$, $q(\hat{\rho} = 0.4)$, and β_N. It also shows how the controller finds, on its own, trends for the actuator trajectories very similar to those from the target shot.

4.2.2. Simulation study 2: shot modification using β_N + interior q-profile control. Both in present devices and future

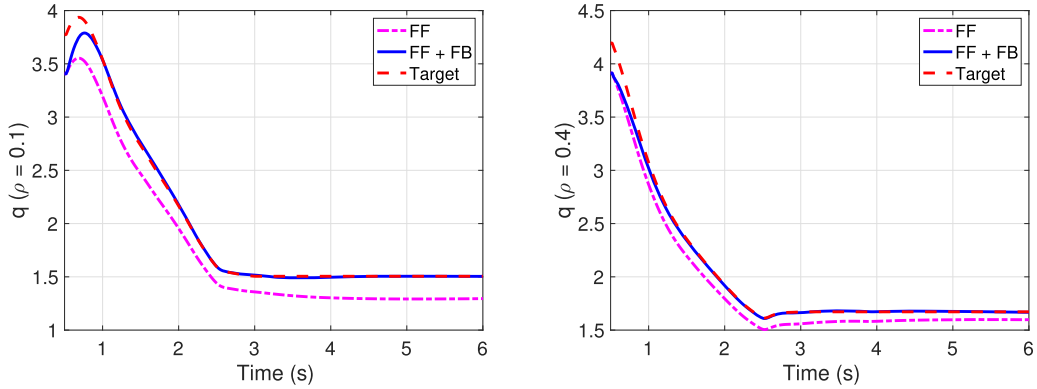

Figure 8. Simulation study 2: time evolutions for q at $\hat{\rho} = 0.10, 0.40$ in FF-only (dashed-dotted magenta) and FF + FB (solid blue) simulations, together with the target q^{tar} (dashed red). Good tracking at both interior nodes is achieved by raising and shaping the q profile by means of FB control.

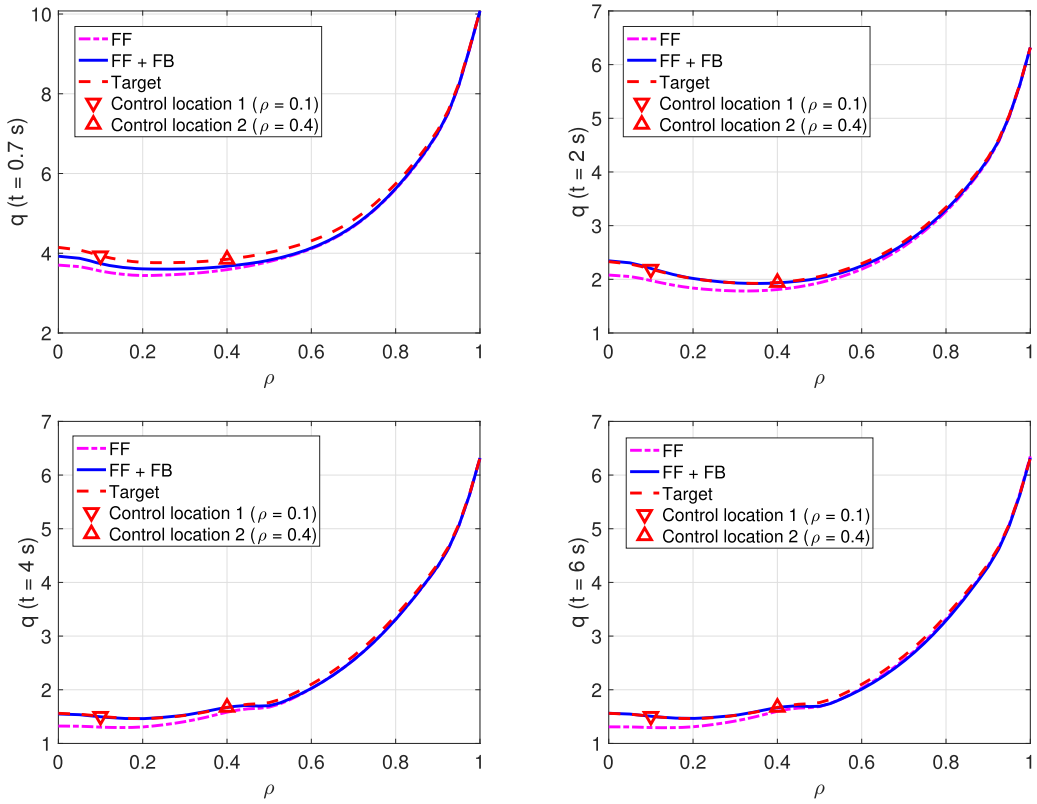

Figure 9. Simulation study 2: comparison of q profiles at $t = 0.7$, 2, 4, and 6 s in FF-only (dashed-dotted magenta) and FF + FB (solid blue) simulations, together with the target q^{tar} (dashed red) and spatial locations for interior q-profile control (red triangles). Very low magnetic shear (≈ 0) is achieved in the region $\hat{\rho} \leqslant 0.2$.

reactor-grade tokamaks, and due to physical and technological reasons, it may be convenient (or even mandatory) to have a predetermined I_{p} trajectory. Therefore, regulation of the q profile by means of boundary control may not be an available actuation method. The goal of this second simulation study is to show how the controller is capable of modifying the q-profile and β_N evolutions from shot 147 634 only by means of diffusion control (i.e., P_{tot} control) and interior control (i.e., $P_{\text{NBI,ON}}$, $P_{\text{NBI,OFF}}$, and P_{EC} control). In this simulation case the experimental evolution of I_{p} from shot 147 634, shown in figure 2 (right), is adopted. Targets for q and β_N are generated from q^{exp} and β_N^{exp}, respectively, as

$$q^{\text{tar}} = (1.12 - 0.12\hat{\rho})q^{\text{exp}}, \quad \beta_N^{\text{tar}} = 1.06\beta_N^{\text{exp}}, \tag{73}$$

when $t \leqslant 3$ s, and as

$$q^{\text{tar}} = (1.12 - 0.12\hat{\rho})q^{\text{exp}}(t = 3\,\text{s}), \quad \beta_N^{\text{tar}} = 1.06\beta_N^{\text{exp}}(t = 3\ \text{s}), \tag{74}$$

when $t > 3$ s, i.e., the q-profile and β_N targets are kept constant in time after 3 s. In this simulation study, the experimental actuator trajectories from shot 147 634 used to predict q^{exp} and β_N^{exp} are adopted as the FF inputs. Figures 7–10 compare the

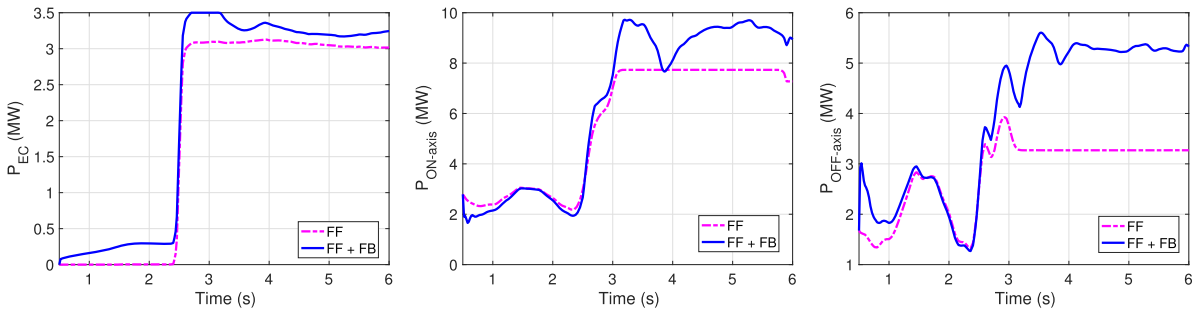

Figure 10. Simulation study 2: time evolutions for P_{EC}, $P_{\mathrm{NBI,ON}}$, and $P_{\mathrm{NBI,OFF}}$ in FF-only (dashed-dotted magenta) and FF + FB (solid blue) simulations.

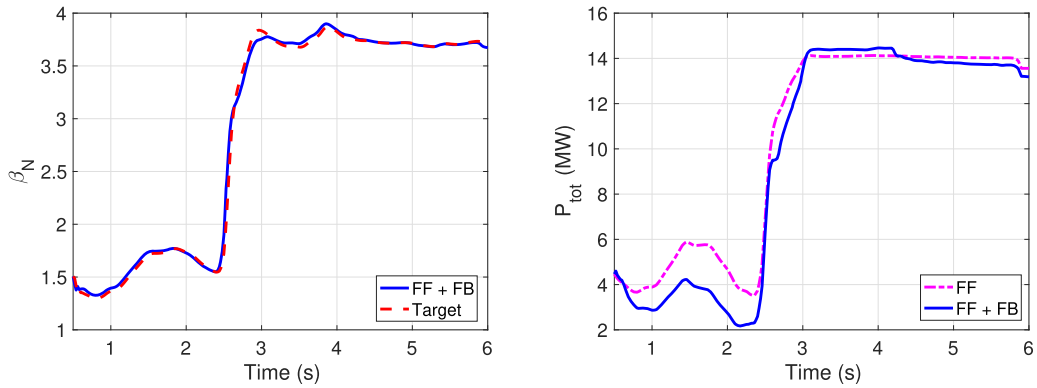

Figure 11. Simulation study 3: time evolutions for β_N and P_{tot} in FF-only (dashed-dotted magenta) and FF + FB (solid blue) simulations, together with the target β_N^{tar} (dashed red). The FF evolution for β_N is not shown because it is identical to β_N^{tar}.

abilities of both the FF-only and the FF + FB controllers to track the desired targets. In the latter case, the FB component of the controller corrects the FF inputs, which are identical to the experimental inputs from shot 147 634, to effectively track q^{tar} and β_N^{tar}, which are modified versions of the q and β_N predicted in simulations by using the experimental inputs from shot 147 634 (i.e., modified versions of q^{exp} and β_N^{exp} as given by (73) and (74)).

Figure 7 shows the β_N and P_{tot} evolutions, figure 8 shows the q-profile evolutions at $\hat{\rho} = 0.1$ and $\hat{\rho} = 0.4$, figure 9 shows the q profiles at $t = 0.7$ s, 2 s, 4 s, and 6 s, and figure 10 shows the NBI and EC power trajectories. These plots demonstrate the FB controller's capability to simultaneously regulate β_N and q at $\hat{\rho} = 0.1$ and $\hat{\rho} = 0.4$. In order to increase β_N towards β_N^{tar}, the controller increases P_{tot} during the whole simulation (see figure 7). The increase in β_N is correlated with an increase in T_{e}, which implies a decrease in η, and contributes to a rise of q in the region $\hat{\rho} \lessapprox 0.5$ (see figure 9). In the outer region $\hat{\rho} \gtrapprox 0.5$, the effect of P_{tot} is significantly smaller. This was expected because the auxiliary sources normally heat and drive current at the innermost part of the plasma, making I_{p} modulation (not considered in this simulation study) the dominant actuation mechanism for the outer region of the current profile. The regulation of q at $\hat{\rho} = 0.1$ and $\hat{\rho} = 0.4$ is successfully carried out (see figure 8) by modulating $P_{\mathrm{NBI,ON}}$, $P_{\mathrm{NBI,OFF}}$, and P_{EC} (see figure 10) while delivering the P_{tot} needed for β_N control. A good matching of the desired q^{tar} profile is achieved within the $\hat{\rho} \lessapprox 0.5$ region, delivering very low magnetic shear in the $\hat{\rho} \leqslant 0.2$ region. However, a match of the whole target profile is not observed in this simulation case. This is a consequence of the arbitrariness of the chosen target profile. It is important to realize that q^{tar} was obtained by arbitrarily modifying q^{exp}. While it is guaranteed that q^{exp} is physically feasible, there is no such guarantee for q^{tar}. However, the controllability properties of the system guarantee that this arbitrary target profile can indeed be tracked at two spatial locations, as confirmed by the simulation results. It must also be noted that, although q achieves an almost stationary value, the controller requests some fluctuations in $P_{\mathrm{NBI,ON}}$, $P_{\mathrm{NBI,OFF}}$, and P_{EC}. This happens because, due to the n_{e} and T_{e} variations normally found during the discharge (due to small fluctuations in both q and $\bar{n}_{\mathrm{e}}$), the controller must vary the power of the auxiliary sources to obtain the desired auxiliary-source-driven currents.

4.2.3. Simulation study 3: shot modification using interior q-profile control. In addition to keeping a predetermined I_{p} trajectory, it may be of interest to maintain a particular β_N evolution already proven experimentally to ensure MHD stability. For instance, increasing the target for β_N as done in the previous simulation study may also increase the risk of triggering MHD instabilities, which can lead to a decrease in plasma performance and eventually to a plasma disruption with the potential of machine damages. The goal of this third simulation study is to demonstrate the FB controller's capability of modifying q from shot 147 634 while keeping the same β_N evolution. As in the previous simulation case, the I_{p} evolution from shot 147 634 is maintained, and the regulation of q at

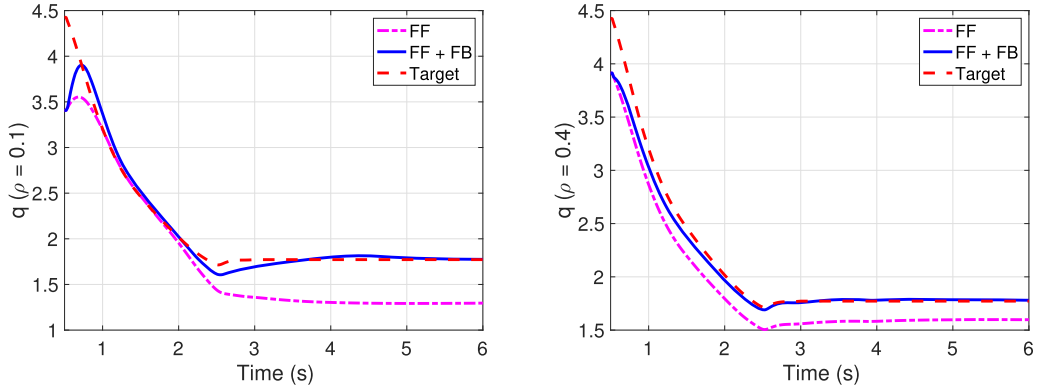

Figure 12. Simulation study 3: time evolutions for q at $\hat{\rho} = 0.10, 0.40$ in FF-only (dashed-dotted magenta) and FF + FB (solid blue) simulations, together with the target q^{tar} (dashed red). Although tracking could be improved if actuator saturation were not present during some periods of time, convergence towards q^{tar} is achieved.

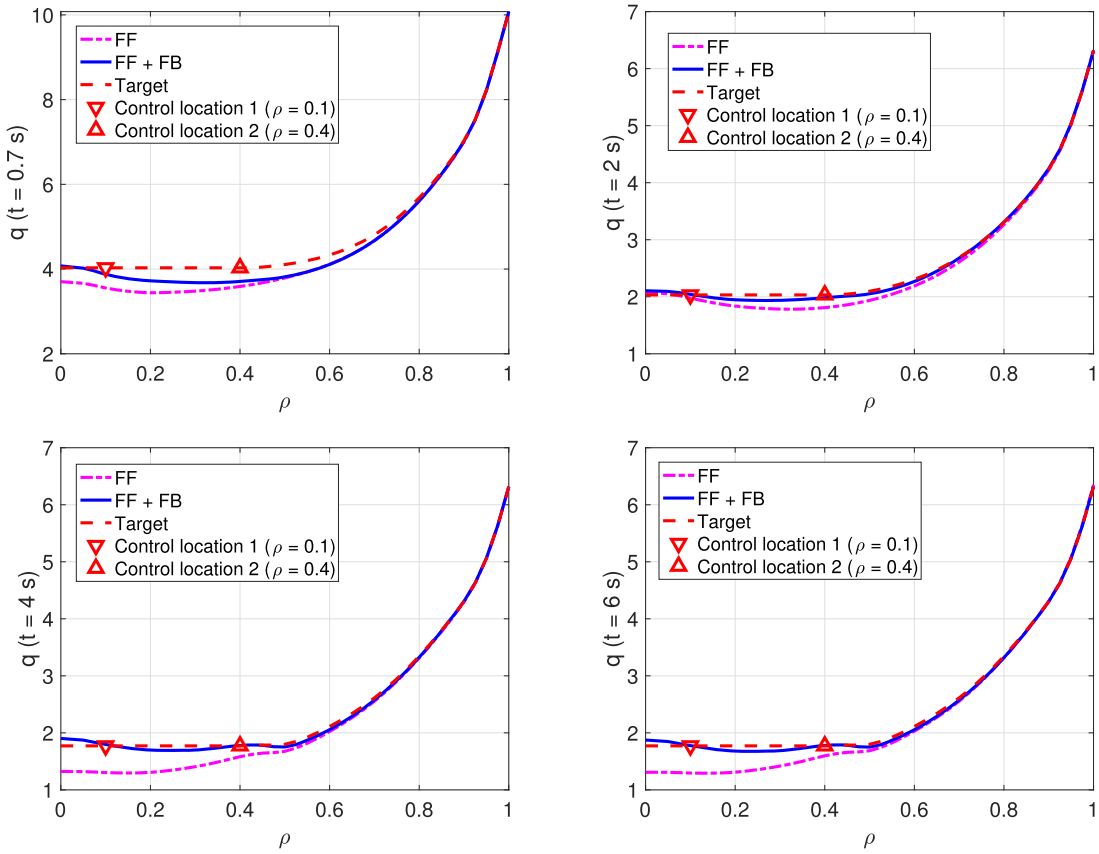

Figure 13. Simulation study 3: comparison of q profiles at $t = 0.7$, 2, 4, and 6 s in FF-only (dashed-dotted magenta) and FF + FB (solid blue) simulations, together with the target q^{tar} (dashed red) and spatial locations for interior q-profile control (red triangles).

the two control points is achieved only by means of interior control (i.e., $P_{\text{NBI,ON}}$, $P_{\text{NBI,OFF}}$, and P_{EC} control) while regulating β_N around β_N^{exp} by using diffusion control (i.e., P_{tot} control).

Whereas the β_N evolution predicted by the inputs from shot 147 634 is adopted as the β_N target, i.e., $\beta_N^{\text{tar}} = \beta_N^{\text{exp}}$, the q-profile target is chosen as

$$q^{\text{tar}} = \left[1 + 0.33(\hat{\rho} - 1)^2\right] q^{\text{exp}}, \quad \text{if } \hat{\rho} \geqslant 0.4 \tag{75}$$

$$q^{\text{tar}} = q^{\text{tar}}(\hat{\rho} = 0.4), \quad \text{if } \hat{\rho} < 0.4 \tag{76}$$

if $t \leqslant 3$ s, and as

$$q^{\text{tar}} = \left[1 + 0.33(\hat{\rho} - 1)^2\right] q^{\text{exp}}(t = 3 \text{ s}), \quad \text{if } \hat{\rho} \geqslant 0.4 \tag{77}$$

$$q^{\text{tar}} = q^{\text{tar}}(\hat{\rho} = 0.4, t = 3 \text{ s}), \quad \text{if } \hat{\rho} < 0.4 \tag{78}$$

if $t > 3$ s. This choice represents a q-profile shape that is significantly more challenging to achieve than the one chosen in the previous simulation study. It should be noted that q^{tar} in (75)–(78) depends on $\hat{\rho}^2$ and sets the goal of raising $q(\hat{\rho} = 0)$

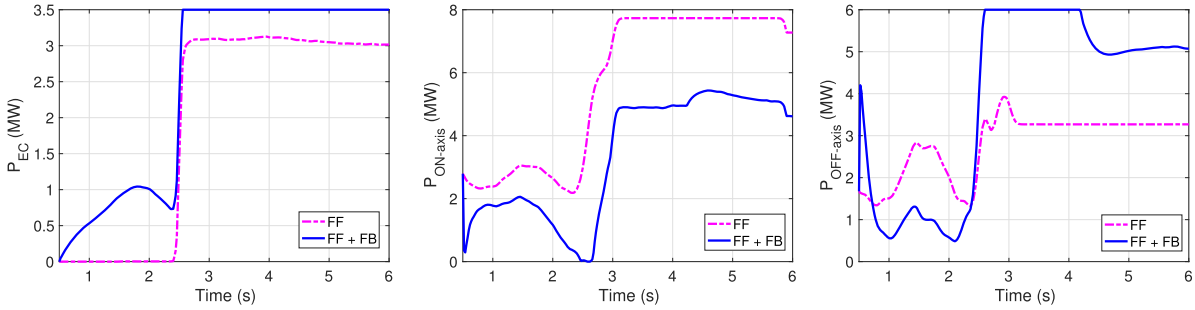

Figure 14. Simulation study 3: time evolutions for P_{EC}, $P_{\mathrm{NBI,ON}}$, and $P_{\mathrm{NBI,OFF}}$ in FF-only (dashed-dotted magenta) and FF + FB (solid blue), together with the experimental inputs from shot 147 634 (dashed-red target). Whereas $P_{\mathrm{NBI,ON}}$ is reduced, $P_{\mathrm{NBI,OFF}}$ and P_{EC} are substantially increased and saturate for some periods of time.

a 33% with respect to the value obtained from the simulation for shot 147 634.

In this simulation study, the experimental actuator trajectories from shot 147 634 used to predict q^{exp} and β_N^{exp} are once again adopted as the FF inputs. Figures 11–14 compare the abilities of both the FF-only and the FF + FB controllers to track the desired targets. In the latter case, the FB component of the controller corrects the FF inputs to effectively track q^{tar} and β_N^{tar}. While q^{tar} is a modified version of q^{exp}, as given by (75)–(78), β_N^{tar} is identical to β_N^{exp}. Figure 11 shows the β_N and P_{tot} evolutions, figure 12 shows the q-profile evolutions at $\hat{\rho} = 0.1$ and $\hat{\rho} = 0.4$, figure 13 shows the q profiles at $t = 0.7$ s, 2 s, 4 s, and 6 s, and figure 14 shows the NBI and EC power trajectories. The FB controller's capability to regulate q at $\hat{\rho} = 0.1$ and $\hat{\rho} = 0.4$ by interior actuation only, while keeping the β_N evolution from shot 147 634, is shown in figures 11 and 12. This is achieved by modulating the NBI and EC powers, in such a way that $P_{\mathrm{NBI,ON}}$ is decreased while $P_{\mathrm{NBI,OFF}}$ and P_{EC} are increased (see figure 14), so that q is raised in the region $\hat{\rho} \lessapprox 0.5$ (see figure 13). In fact, $P_{\mathrm{NBI,OFF}}$ and P_{EC} are saturated for a good part of the simulation (see figure 14), making it difficult to accurately control $q(\hat{\rho} = 0.1)$ and $q(\hat{\rho} = 0.4)$ during some parts of the simulation. This is a natural result of employing the very demanding q-profile target (75)–(78), which requires a significant increase of q in the inner part of the plasma. However, it can be appreciated that, during most of the simulation, a lower P_{tot} suffices to achieve the same β_N as in shot 147 634 (see figure 11). This suggests a plasma-confinement improvement due to q-profile shaping (achieving negative magnetic shear in the region $\hat{\rho} \lessapprox 0.25$), which is consistent with some experimental observations in negative shear AT scenarios [2]. It can be observed, nonetheless, that the q-profile shape in the region $\hat{\rho} \lessapprox 0.5$ is in general not the same as the target q^{tar}. As discussed for the previous case, this happens because of the arbitrariness of the chosen q^{tar} and the controllability limits guaranteeing regulation only at two interior points ($\hat{\rho} = 0.1$ and $\hat{\rho} = 0.4$).

5. Conclusions and possible future work

A robust, nonlinear, model-based controller has been presented in this work for simultaneous q-profile + β_N control. By means of 1D simulations for a DIII-D H-mode scenario, the capability of the controller to change the q-profile shape, sometimes in conjunction with β_N and q_{edge} regulation, has been demonstrated. FB linearization techniques allow for a very intuitive assessment of the actuation capability for q-profile + β_N control within a tokamak, providing a quantification of controllability based on both the total number of auxiliary sources and their current deposition profiles. Robustification techniques using Lyapunov redesign ensure that the error dynamics remains bounded despite very general uncertainties included in the modeling process. In other words, Lyapunov redesign reduces the level of model accuracy needed to guarantee acceptable closed-loop performance. The proposed robust controller is capable of rejecting a variety of disturbances, including MHD events, due to the FB mechanism. The performance of the controller in presence of MHD disturbances will depend however on how they affect the efficiency of the actuation mechanisms and the plasma dynamics. Simultaneous regulation of β_N and the q-profile shape may allow for improving plasma performance, confinement, and steadiness while avoiding MHD instabilities, which is an important goal in fusion research. Future work includes experimental testing of the control algorithm in DIII-D.

Acknowledgments

This work was supported by the US Department of Energy under contract DE-SC0010661.

Appendix A. Details of the model for the θ dynamics

By taking derivative in the MDE, equation (2), with respect to $\hat{\rho}$,

$$\frac{\partial}{\partial\hat{\rho}}\left(\frac{\partial\psi}{\partial t}\right) = \frac{\partial}{\partial\hat{\rho}}\left[\frac{\eta}{\mu_0\rho_b^2\hat{F}^2}\frac{1}{\hat{\rho}}\frac{\partial}{\partial\hat{\rho}}\left(\hat{\rho}D_\psi\frac{\partial\psi}{\partial\hat{\rho}}\right)\right] + \frac{\partial}{\partial\hat{\rho}}\left[\eta R_0\hat{H}j_{\mathrm{ni}}\right], \tag{A.1}$$

and introducing the definition of the poloidal flux gradient, $\theta \triangleq \frac{\partial\psi}{\partial\hat{\rho}}$, and the definition for j_{ni} in equation (4), the application of

the chain rule leads to

$$\frac{\partial\theta}{\partial t} = \frac{1}{\mu_0\rho_b^2}\left\{\frac{\partial\left(\frac{\eta}{\hat{F}^2}\right)}{\partial\hat{\rho}}\left[\left(\frac{D_\psi}{\hat{\rho}}+D'_\psi\right)\theta + D_\psi\theta'\right] + \frac{\eta}{\hat{F}^2}\frac{\partial}{\partial\hat{\rho}}\left[\left(\frac{D_\psi}{\hat{\rho}}+D'_\psi\right)\theta + D_\psi\theta'\right]\right\} + \sum_{i=1}^{i=N_{\text{aux}}} R_0\frac{\partial}{\partial\hat{\rho}}\left[\eta\hat{H}j_{\text{aux}}\right] + R_0\frac{\partial}{\partial\hat{\rho}}\left[\eta\hat{H}j_{\text{BS}}\right], \quad \text{(A.2)}$$

where the index ($'$) denotes derivative with respect to $\hat{\rho}$. Further development of the first two terms in equation (A.2) yield

$$\frac{\partial}{\partial\hat{\rho}}\left(\frac{\eta}{\hat{F}^2}\right)\left[\left(\frac{D_\psi}{\hat{\rho}}+D'_\psi\right)\theta + D_\psi\theta'\right] = \left[\frac{\eta'}{\hat{F}^2} - 2\frac{\hat{F}'\eta}{\hat{F}^3}\right]\left[\left(\frac{D_\psi}{\hat{\rho}}+D'_\psi\right)\theta + D_\psi\theta'\right],$$

$$\frac{\partial}{\partial\hat{\rho}}\left[\left(\frac{D_\psi}{\hat{\rho}}+D'_\psi\right)\theta + D_\psi\theta'\right] = \left[\left(\frac{\hat{\rho}D'_\psi - D_\psi}{\hat{\rho}^2}+D''_\psi\right)\theta + \left(\frac{D_\psi}{\hat{\rho}}+2D'_\psi\right)\theta' + D_\psi\theta''\right],$$

so equation (A.2) can be rewritten as

$$\frac{\partial\theta}{\partial t} = \frac{1}{\mu_0\rho_b^2}\left[\left(\frac{\eta'}{\hat{F}^2} - 2\frac{\hat{F}'\eta}{\hat{F}^3}\right)\left(\frac{D_\psi}{\hat{\rho}}+D'_\psi\right) + \frac{\eta}{\hat{F}^2}\left(\frac{\hat{\rho}D'_\psi - D_\psi}{\hat{\rho}^2}+D''_\psi\right)\right]\theta + \frac{1}{\mu_0\rho_b^2}\left[\left(\frac{\eta'}{\hat{F}^2} - 2\frac{\hat{F}'\eta}{\hat{F}^3}\right)D_\psi + \frac{\eta}{\hat{F}^2}\left(\frac{D_\psi}{\hat{\rho}}+2D'_\psi\right)\right]\theta' + \frac{1}{\mu_0\rho_b^2}\left[\frac{\eta}{\hat{F}^2}D_\psi\right]\theta'' + R_0\frac{\partial}{\partial\hat{\rho}}\left[\eta\hat{H}j_{\text{aux}}\right] + R_0\frac{\partial}{\partial\hat{\rho}}\left[\eta\hat{H}j_{\text{BS}}\right]. \quad \text{(A.3)}$$

The expression for η in (4) and its derivative with respect to $\hat{\rho}$ can be rewritten as

$$\eta = g_\eta(\hat{\rho})u_\eta(t), \quad \eta' = g'_\eta(\hat{\rho})u_\eta(t), \quad \text{(A.4)}$$

where $g_\eta(\hat{\rho}) \triangleq \frac{k_{\text{sp}}(\hat{\rho})Z_{\text{eff}}}{\left(T_{\text{e}}^{\text{prof}}(\hat{\rho})n_{\text{e}}^{\text{prof}}(\hat{\rho})^\zeta\right)^{3/2}}$ and $u_\eta(t) \triangleq I_{\text{p}}(t)^{\frac{-3\gamma}{2}} P_{\text{tot}}(t)^{\frac{-3\epsilon}{2}}\bar{n}_{\text{e}}(t)^{\frac{-3\zeta}{2}}$. By defining

$$h_{11}(\hat{\rho}) \triangleq \frac{1}{\mu_0\rho_b^2}\frac{g_\eta}{\hat{F}^2}D_\psi, \quad \text{(A.5)}$$

$$h_{12}(\hat{\rho}) \triangleq \frac{1}{\mu_0\rho_b^2}\left[\left(\frac{g'_\eta}{\hat{F}^2} - 2\frac{\hat{F}'g_\eta}{\hat{F}^3}\right)D_\psi + \frac{g_\eta}{\hat{F}^2}\left(\frac{D_\psi}{\hat{\rho}}+2D'_\psi\right)\right], \quad \text{(A.6)}$$

$$h_{13}(\hat{\rho}) \triangleq \frac{1}{\mu_0\rho_b^2}\left[\left(\frac{g'_\eta}{\hat{F}^2} - 2\frac{\hat{F}'g_\eta}{\hat{F}^3}\right)\left(\frac{D_\psi}{\hat{\rho}}+D'_\psi\right) + \frac{g_\eta}{\hat{F}^2}\left(\frac{\hat{\rho}D'_\psi - D_\psi}{\hat{\rho}^2}+D''_\psi\right)\right], \quad \text{(A.7)}$$

it is found that equation (A.3) can be rewritten as

$$\frac{\partial\theta}{\partial t} = \left[h_{11}(\hat{\rho})\theta'' + h_{12}(\hat{\rho})\theta' + h_{13}(\hat{\rho})\theta\right]u_\eta(t) + R_0\frac{\partial}{\partial\hat{\rho}}\left[\eta\hat{H}j_{\text{aux}}\right] + R_0\frac{\partial}{\partial\hat{\rho}}\left[\eta\hat{H}j_{\text{BS}}\right]. \quad \text{(A.8)}$$

The expression in (5) related to the auxiliary-source driven current, j_{aux}, can be rewritten using the models for T_{e} and n_{e} given in (7) and (8) as

$$j_{\text{aux}} = \sum_{i=1}^{i=N_{\text{NBI}}} g_{\text{NBI},i}(\hat{\rho})u_{\text{NBI},i}(t) + g_{\text{EC}}(\hat{\rho})u_{\text{EC}}(t), \quad \text{(A.9)}$$

where

$$g_{\text{NBI},i}(\hat{\rho}) \triangleq j_{\text{NBI}}^{\text{prof}}(\hat{\rho})\frac{g(\hat{\rho})^{\lambda_{\text{NB}}}}{n_{\text{e}}^{\text{prof}}(\hat{\rho})}, \quad g_{\text{EC}}(\hat{\rho}) \triangleq j_{\text{EC}}^{\text{prof}}(\hat{\rho})\frac{g(\hat{\rho})^{\lambda_{\text{EC}}}}{n_{\text{e}}^{\text{prof}}(\hat{\rho})}, \quad \text{(A.10)}$$

$$u_{\text{NBI},i} \triangleq I_{\text{p}}^{\gamma\left(\lambda_{\text{NBI}}-\frac{3}{2}\right)}P_{\text{tot}}^{\epsilon\left(\lambda_{\text{NBI}}-\frac{3}{2}\right)}\bar{n}_{\text{e}}^{\zeta\left(\lambda_{\text{NBI}}-\frac{3}{2}\right)-1}P_{\text{NBI},i}, \quad \text{(A.11)}$$

$$u_{\text{EC}} \triangleq I_{\text{p}}^{\gamma\left(\lambda_{\text{EC}}-\frac{3}{2}\right)}P_{\text{tot}}^{\epsilon\left(\lambda_{\text{EC}}-\frac{3}{2}\right)}\bar{n}_{\text{e}}^{\zeta\left(\lambda_{\text{EC}}-\frac{3}{2}\right)-1}P_{\text{EC}}, \quad \text{(A.12)}$$

with $g(\hat{\rho}) \triangleq T_{\text{e}}^{\text{prof}}(\hat{\rho})n_{\text{e}}^{\text{prof}}(\hat{\rho})^\zeta$. Then, the second term on the right-hand side of (A.8) becomes

$$R_0\frac{\partial}{\partial\hat{\rho}}\left[\eta\hat{H}j_{\text{aux}}\right] = \sum_{i=1}^{i=N_{\text{NBI}}} R_0\frac{\partial}{\partial\hat{\rho}}\left[\hat{H}g_\eta(\hat{\rho})g_{\text{NBI},i}(\hat{\rho})\right]u_{\text{NBI},i}(t) + R_0\frac{\partial}{\partial\hat{\rho}}\left[\hat{H}g_\eta(\hat{\rho})g_{\text{EC}}(\hat{\rho})\right]u_{\text{EC}}(t), \quad \text{(A.13)}$$

and defining

$$h_{\text{NBI},i}(\hat{\rho}) \triangleq R_0\frac{\partial\left(\hat{H}g_\eta(\hat{\rho})g_{\text{NBI},i}(\hat{\rho})\right)}{\partial\hat{\rho}}, \quad h_{\text{EC}}(\hat{\rho}) \triangleq R_0\frac{\partial\left(\hat{H}g_\eta(\hat{\rho})g_{\text{EC}}(\hat{\rho})\right)}{\partial\hat{\rho}}, \quad \text{(A.14)}$$

then (A.13) becomes

$$R_0\frac{\partial}{\partial\hat{\rho}}\left[\eta\hat{H}j_{\text{aux}}\right] = \sum_{i=1}^{i=N_{\text{NBI}}} h_{\text{NBI},i}(\hat{\rho})u_{\text{NBI},i}(t) + h_{\text{EC}}(\hat{\rho})u_{\text{EC}}(t). \quad \text{(A.15)}$$

In order to rewrite the last term on the right-hand side of equation (A.8), j_{BS} given by equation (6) can be expressed, using the definition of θ and equations (7)–(8), as

$$j_{\rm BS} = \frac{R_0}{\hat{F}(\hat{\rho})}\frac{1}{\theta}\left[2\mathcal{L}_{31}(\hat{\rho})g(\hat{\rho})\left[n_{\rm e}^{\rm prof}(\hat{\rho})\right]' + (2\mathcal{L}_{31}+\mathcal{L}_{32}+\alpha\mathcal{L}_{34})n_{\rm e}^{\rm prof}(\hat{\rho})g'(\hat{\rho})\right] \times I_{\rm p}(t)^{\gamma}P_{\rm tot}(t)^{\epsilon}\bar{n}_{\rm e}(t)^{\zeta+1}, \quad (A.16)$$

and therefore, the last term in (A.8) becomes

$$R_0\frac{\partial}{\partial\hat{\rho}}\left[\eta\hat{H}j_{\rm BS}\right] = \frac{\partial}{\partial\hat{\rho}}\left[R_0\hat{H}g_{\eta}(\hat{\rho})\frac{R_0}{\hat{F}(\hat{\rho})}\frac{1}{\theta} \times \left[2\mathcal{L}_{31}(\hat{\rho})g(\hat{\rho})[n_{\rm e}^{\rm prof}(\hat{\rho})]' + (2\mathcal{L}_{31}+\mathcal{L}_{32}+\alpha\mathcal{L}_{34})n_{\rm e}^{\rm prof}(\hat{\rho})g'(\hat{\rho})\right]\right] \times I_{\rm p}(t)^{-\gamma/2}P_{\rm tot}(t)^{-\epsilon/2}\bar{n}_{\rm e}(t)^{-\zeta/2+1}. \quad (A.17)$$

By defining

$$h_{\rm BS}(\hat{\rho}) \triangleq \hat{H}g_{\eta}\frac{R_0}{\hat{F}}\left[2\mathcal{L}_{31}g[n_{\rm e}^{\rm prof}]' + (2\mathcal{L}_{31}+\mathcal{L}_{32}+\alpha\mathcal{L}_{34})n_{\rm e}^{\rm prof}g'\right] \quad (A.18)$$

$$u_{\rm BS}(t) \triangleq I_{\rm p}(t)^{-\gamma/2}P_{\rm tot}(t)^{-\epsilon/2}\bar{n}_{\rm e}(t)^{-\zeta/2+1}, \quad (A.19)$$

equation (A.17) can be rewritten as

$$R_0\frac{\partial}{\partial\hat{\rho}}\left[\hat{H}\eta(T_{\rm e})j_{\rm BS}\right] = \frac{\partial}{\partial\hat{\rho}}\left[\frac{h_{\rm BS}(\hat{\rho})}{\theta}\right]u_{\rm BS}(t), \quad (A.20)$$

and the MDE (A.8) adopts the following shape

$$\frac{\partial\theta}{\partial t} = \left[h_{11}\theta'' + h_{12}\theta' + h_{13}\theta\right]u_{\eta} + \sum_{i=1}^{i=N_{\rm NBI}}h_{{\rm NBI},i}u_{{\rm NBI},i} + h_{\rm EC}u_{\rm EC} + \frac{\partial}{\partial\hat{\rho}}\left[\frac{h_{\rm BS}}{\theta}\right]u_{\rm BS}. \quad (A.21)$$

The finite differences method is employed to discretize equation (A.21) in the $\hat{\rho}$ domain. A total number $N+1$ nodes are used within the interval $\hat{\rho}=[0,1]$. For the mth inner node ($m=1,2,\ldots,N-1$), the equation that gives the evolution of the θ profile is given by

$$\frac{\partial\theta(\hat{\rho}_m,t)}{\partial t} = \left[h_{13}(\hat{\rho}_m)\theta(\hat{\rho}_m,t) + h_{12}(\hat{\rho}_m)\frac{\theta(\hat{\rho}_{m+1},t)-\theta(\hat{\rho}_{m-1},t)}{2\Delta\hat{\rho}} + h_{11}(\hat{\rho}_m)\frac{\theta(\hat{\rho}_{m+1},t)+\theta(\hat{\rho}_{m-1},t)-2\theta(\hat{\rho}_m,t)}{\Delta\hat{\rho}^2}\right]u_{\eta}(t) + \sum_{i=1}^{i=N_{\rm aux}}h_{{\rm aux},i}(\hat{\rho}_m)u_{{\rm aux},i}(t) + \left[\frac{1}{\theta(\hat{\rho}_m)}\frac{{\rm d}h_{\rm BS}}{d\hat{\rho}}(\hat{\rho}_m) - \frac{h_{\rm BS}(\hat{\rho}_m)}{\theta(\hat{\rho}_m)^2}\frac{\theta(\hat{\rho}_{m+1},t)-\theta(\hat{\rho}_{m-1},t)}{2\Delta\hat{\rho}}\right]u_{\rm BS}(t), \quad (A.22)$$

where $\hat{\rho}_m = m\Delta\hat{\rho}$ and $\Delta\hat{\rho}=1/N$. Re-arranging terms, and using the following notation and definitions,

$$\theta_m \triangleq \theta(\hat{\rho}_m,t), \quad (A.23)$$

$$\alpha_m \triangleq h_{13}(\hat{\rho}_m) - \frac{2h_{11}(\hat{\rho}_m)}{\Delta\hat{\rho}},\ \beta_m \triangleq \frac{h_{11}(\hat{\rho}_m)}{\Delta\hat{\rho}^2} + \frac{h_{12}(\hat{\rho}_m)}{2\Delta\hat{\rho}},\ \gamma_m \triangleq \frac{h_{11}(\hat{\rho}_m)}{\Delta\hat{\rho}^2} - \frac{h_{12}(\hat{\rho}_m)}{2\Delta\hat{\rho}}, \quad (A.24)$$

$$h_{{\rm NBI},i}^m \triangleq h_{{\rm NBI},i}(\hat{\rho}_m),\quad h_{\rm EC}^m \triangleq h_{\rm EC}(\hat{\rho}_m),\quad h_{{\rm BS},1}^m \triangleq \frac{{\rm d}h_{\rm BS}}{d\hat{\rho}}(\hat{\rho}_m),\quad h_{{\rm BS},2}^m \triangleq h_{\rm BS}(\hat{\rho}_m), \quad (A.25)$$

equation (A.22) can be written as

$$\dot{\theta}_m = \left[\gamma_m\theta_m + \beta_m\theta_{m+1} + \alpha_m\theta_{m-1}\right]u_{\eta}(t) + \sum_{i=1}^{i=N_{\rm NBI}}h_{{\rm NBI},i}^m u_{{\rm NBI},i}(t) + h_{\rm EC}^m u_{\rm EC}(t) + \left[\frac{1}{\theta_m}h_{{\rm BS},1}^m - \frac{h_{{\rm BS},2}^m}{\theta_m^2}\frac{\theta_{m+1}-\theta_{m-1}}{2\Delta\hat{\rho}}\right]u_{\rm BS}(t). \quad (A.26)$$

The application of equation (A.26) at each of the inner nodes ($m=1,2,\ldots,N-1$) yields a set of $N-1$ equations that, together with the boundary conditions $\theta_0=0$ and $\theta_N=-k_{I_{\rm p}}^*I_{\rm p}(t)$, closes the model that defines the evolution of θ at the $N+1$ nodes. For the inner nodes, the system can be written in matrix form as

$$\dot{\theta} = G(\theta,I_{\rm p})u, \quad (A.27)$$

where $\theta=[\theta_1,\theta_2,\ldots,\theta_m,\ldots,\theta_{N-1}]^T\in\mathbb{R}^{(N-1)\times 1}$, $u=[u_{\eta}(t), u_{{\rm NBI},1}(t), u_{{\rm NBI},2}(t),\ldots, u_{{\rm NBI},N_{\rm NBI}}(t), u_{\rm EC}(t), u_{\rm BS}(t)]^T\in\mathbb{R}^{(N_{\rm NBI}+3)\times 1}$, and $G(\theta,I_{\rm p})\in\mathbb{R}^{(N-1)\times(N_{\rm NBI}+3)}$ is given by

$$G = \begin{bmatrix} \alpha_1\theta_0+\beta_1\theta_2+\gamma_1\theta_1 & h_{{\rm NBI},1}^1 & \cdots & h_{\rm EC}^1 & \frac{h_{{\rm BS},1}^1}{\theta_1} - \frac{h_{{\rm BS},2}^1}{\theta_1^2}\frac{\theta_2-\theta_0}{2\Delta\hat{\rho}} \\ \vdots & \vdots & \ddots & \vdots & \vdots \\ \alpha_m\theta_{m-1}+\beta_m\theta_{m+1}+\gamma_m\theta_m & h_{{\rm NBI},1}^m & \cdots & h_{\rm EC}^m & \frac{h_{{\rm BS},1}^m}{\theta_m} - \frac{h_{{\rm BS},2}^m}{\theta_m^2}\frac{\theta_{m+1}-\theta_{m-1}}{2\Delta\hat{\rho}} \\ \vdots & \vdots & \ddots & \vdots & \vdots \\ \alpha_{N-1}\theta_{N-2}-\beta_{N-1}k_{I_{\rm p}}I_{\rm p}-\gamma_{N-1}\theta_{N-1} & h_{{\rm NBI},1}^{N-1} & \cdots & h_{\rm EC}^{N-1} & \frac{h_{{\rm BS},1}^{N-1}}{\theta_{N-1}} - \frac{h_{{\rm BS},2}^{N-1}}{\theta_{N-1}^2}\frac{-k_{I_{\rm p}}I_{\rm p}-\theta_{N-2}}{2\Delta\hat{\rho}} \end{bmatrix}.$$

Appendix B. Lyapunov theory basics

The Lyapunov stability theory is the basis of the controller design shown in this paper. Consider a nonlinear, autonomous system

$$\dot{x} = g(x,u), \quad (B.1)$$

where $x\in\mathbb{R}^n$ is the state vector, $u\in\mathbb{R}^p$ is the input vector, and $g:\mathbb{R}^n\times\mathbb{R}^p\to\mathbb{R}^n$ is a nonlinear function. It is assumed that a control law $u=u^{\rm nom}(x)$ is known and set such that $g(x,u^{\rm nom}(x))\triangleq f(x)$, and also that the resulting function

$f:\mathbb{R}^n \to \mathbb{R}^n$ is locally Lipschitz. It is said that $x = \bar{x}$ is an equilibrium of the system if

$$f(\bar{x}) = 0. \tag{B.2}$$

Without loss of generality, it is possible to use the change of variables $\tilde{x} = x - \bar{x}$ so that (B.1) can be rewritten as

$$\dot{\tilde{x}} = f(\tilde{x}), \tag{B.3}$$

which is a system with an equilibrium at the origin. It is necessary to define stability, asymptotical stability, and global asymptotical stability of an equilibrium. The equilibrium $\tilde{x} = 0$ of the system (B.3) is stable if, for each $\epsilon > 0$, there exists $\delta = \delta(\epsilon) > 0$ such that

$$\|\tilde{x}(0)\| < \delta \Rightarrow \|\tilde{x}(t)\| < \epsilon, \quad \forall t \geqslant 0. \tag{B.4}$$

Such equilibrium is asymptotically stable if it is stable and δ can be found such that

$$\|\tilde{x}(0)\| < \delta \Rightarrow \lim_{t\to\infty} \tilde{x}(t) = 0, \tag{B.5}$$

and it is globally asymptotically stable if $\|\tilde{x}(0)\|$ can be taken arbitrarily large.

The main Lyapunov theorem exploited in this work for the design of nominal control laws says that, if a continuously differentiable function $V:\mathbb{R}^n \to \mathbb{R}$ can be found for the system (B.3) such that

$$V(0) = 0, \tag{B.6}$$

$$V(\tilde{x}) > 0, \quad \forall\ \tilde{x} \neq 0, \tag{B.7}$$

$$\|\tilde{x}\| \to \infty \Rightarrow V(\tilde{x}) \to \infty, \tag{B.8}$$

$$\dot{V}(x) < 0, \quad \forall\ x \neq 0, \tag{B.9}$$

then the equilibrium $\tilde{x} = 0$ is globally asymptotically stable. If the domain of applicability for the conditions (B.6)–(B.9) is restricted from $\mathbb{R}^n$ to some domain D (for example, because of physical actuator constraints), then globality cannot be claimed. In general, finding the function V, known as Lyapunov function, is a complicated problem. Typical candidates for Lyapunov functions are quadratic functions, $V = \tilde{x}^T P \tilde{x}$ $(P > 0)$, such that $\dot{V} = -\tilde{x}^T Q \tilde{x}$ with $Q > 0$. In this work, the control-design problem is not only finding the Lyapunov functions themselves, which are given by relatively simple quadratic functions, but also finding the stabilizing FB laws $u = u^{\text{nom}}(x)$ at the same time.

A second theorem that is exploited in this work for the design of robust control laws via Lyapunov redesign (see appendix C) says that, if a continuously differentiable function $V:\mathbb{R}^n \to \mathbb{R}$ can be found such that

$$\alpha_1(x) \geqslant V(\tilde{x}) \geqslant \alpha_2(x), \quad \forall\ \tilde{x} \neq 0, \tag{B.10}$$

$$\dot{V}(x) \leqslant -W_3(x), \quad \forall\ \|x\| \geqslant \mu > 0, \tag{B.11}$$

where α_1 is a class $\mathcal{K}$ function[2], α_2 is a class $\mathcal{K}_\infty$ function[3] and $W_3 > 0$ is continuous, and if $\mu < \alpha_2^{-1}(\alpha_1(r))$, for some $r > 0$, then there exists a class $\mathcal{KL}$ function[4] β such that

$$\|\tilde{x}\| \leqslant \beta(\|x(t_0)\|, t - t_0), \quad \forall\ t_0 \leqslant t \leqslant t_0 + T, \tag{B.12}$$

$$\|\tilde{x}\| \leqslant \alpha_2^{-1}(\alpha_1(\mu)), \quad \forall\ t \geqslant t_0 + T, \tag{B.13}$$

for some $T \geqslant 0$ and any initial state $x(t_0)$. When $\alpha_1 = \alpha_2$ can be found, $\|\tilde{x}\|$ is ultimately bounded by μ. A more extensive introduction to Lyapunov stability theory can be found in [17].

Appendix C. Lyapunov redesign basics

Lyapunov redesign is the technique employed in this work to design a robust, nonlinear controller. Consider a nonlinear, autonomous, uncertain system with the following shape

$$\dot{x} = f(x) + G(x)[u + \delta(x,u)], \tag{C.1}$$

where $x \in \mathbb{R}^n$ is the state vector, $u \in \mathbb{R}^p$ is the input vector, $\delta \in \mathbb{R}^p$ is the uncertainty vector, and $f:\mathbb{R}^n \to \mathbb{R}^n$, $G:\mathbb{R}^n \to \mathbb{R}^{n\times p}$ and $\delta:\mathbb{R}^n \times \mathbb{R}^p \to \mathbb{R}^p$ are locally Lipschitz in x and u. It is assumed that a control law $u = u^{\text{nom}}(x)$ and a Lyapunov function $V(x)$ have been found such that the origin of (C.1) is an asymptotically stable equilibrium in closed loop for the nominal system ($\delta = 0$). A control law $u = u^{\text{nom}} + u^{\text{rob}}$ is sought such that (C.1) is asymptotically stable when $\delta \neq 0$. The time derivative of V is given by

$$\dot{V} = \frac{\partial V}{\partial x}(f + Gu^{\text{nom}}) + \frac{\partial V}{\partial x} G\left(u^{\text{rob}} + \delta\right), \tag{C.2}$$

where the dependence on x and u has been dropped to simplify notation. The term $\frac{\partial V}{\partial x}(f + Gu^{\text{nom}})$ corresponds to the time derivative of V when the control law $u = u^{\text{nom}}(x)$ is employed for the nominal system ($\delta \equiv 0$), which is negative by design. Therefore $\frac{\partial V}{\partial x}(f + Gu^{\text{nom}}) < -\alpha_c(\|x\|)$, where α_c is a class $\mathcal{K}$ function. Then, it is found that

$$\dot{V} < -\alpha_c(\|x\|) + \frac{\partial V}{\partial x} G\left(u^{\text{rob}} + \delta\right). \tag{C.3}$$

The term u^{rob} must be designed such that $\dot{V} < 0$, regardless of the value of δ. Using the Cauchy–Schwarz inequality, (C.3) can be rewritten as

$$\dot{V} < -\alpha_c(\|x\|) + \frac{\partial V}{\partial x} G u^{\text{rob}} + \left\| \frac{\partial V}{\partial x} G \right\|_2 \|\delta\|_2. \tag{C.4}$$

If there exists a bound to δ given by

$$\left\|\delta(x, u^{\text{nom}} + u^{\text{rob}})\right\|_2 \leqslant \delta^{\max}, \tag{C.5}$$

[2] A function $f(x)$ belongs to class $\mathcal{K}$ iff (1) it is strictly increasing with x, and (2) $f(0) = 0$.

[3] A function $f(x)$ belongs to class $\mathcal{K}_\infty$ iff (1) it is class $\mathcal{K}$, (2) x can extend to infinity, and (3) $\lim_{x\to\infty} f(x) = \infty$.

[4] A function $f(x,y)$ belongs to class $\mathcal{KL}$ iff (1) for each fixed y^*, the function $f(x,y^*)$ belong to class $\mathcal{K}$ and (2) for each fixed x^*, the function $f(x^*,y)$ is decreasing and tends to zero as $y \to \infty$.

then

$$\dot{V} < -\alpha_c(\|x\|) + \frac{\partial V}{\partial x} G u^{\text{rob}} + \left\| \frac{\partial V}{\partial x} G \right\| \delta^{\max}. \tag{C.6}$$

If u^{rob} is taken as

$$u^{\text{rob}} = -\delta^{\max} \frac{\left(\frac{\partial V}{\partial x} G\right)^T}{\left\| \frac{\partial V}{\partial x} G \right\|_2}, \tag{C.7}$$

then the second-to-last term on the right-hand side of equation (C.6) becomes

$$\frac{\partial V}{\partial x} G u^{\text{rob}} = -\delta^{\max} \left\| \frac{\partial V}{\partial x} G \right\|_2, \tag{C.8}$$

so

$$\dot{V} < -\alpha_c(\|x\|). \tag{C.9}$$

Therefore, all the conditions (B.6)–(B.9) are satisfied, so the origin of (C.1) is asymptotically stable under the control law $u = u^{\text{nom}} + u^{\text{rob}}$, with u^{rob} given by (C.7), as long as a bound (C.5) can be found. Finally, it can be noted that, if G is the identity matrix and $V = \frac{1}{2}\tilde{x}^2$ (as is the case in the derivations shown in this work), $G\frac{\partial V}{\partial x}$ has a pretty simple form, $G\frac{\partial V}{\partial x} = \tilde{x}$.

It must be noted that the control law (C.7) has a singularity at $\left\| \frac{\partial V}{\partial x} G \right\|_2 = 0$, so its practical implementation is limited. In order to avoid this limitation, control law (C.7) is modified as follows. First, a design parameter $\epsilon > 0$ is defined. This parameter ϵ also needs to be small, $\epsilon \to 0$, for reasons that will be shown later in this section. It can be seen that the singularity does not affect the control law (C.7) in the domain defined by $\left\| \frac{\partial V}{\partial x} G \right\|_2 \geqslant \epsilon / \delta^{\max}$. For the domain defined by $\left\| \frac{\partial V}{\partial x} G \right\|_2 < \epsilon / \delta^{\max}$, if the control law is modified as

$$u^{\text{rob}} = -\left(\delta^{\max}\right)^2 \frac{\left(\frac{\partial V}{\partial x} G\right)^T}{\epsilon}, \tag{C.10}$$

then

$$\begin{aligned} \dot{V} &< -\alpha_c(\|x\|) + \frac{\partial V}{\partial x} G u^{\text{rob}} + \left\| \frac{\partial V}{\partial x} G \right\| \delta^{\max} \\ &\leqslant -\alpha_c(\|x\|) - \left(\delta^{\max}\right)^2 \frac{\left\| \frac{\partial V}{\partial x} G \right\|^2}{\epsilon} + \left\| \frac{\partial V}{\partial x} G \right\| \delta^{\max} \\ &\leqslant -\alpha_c(\|x\|) + \frac{\epsilon}{4}, \end{aligned} \tag{C.11}$$

where the fact that $-(\delta^{\max})^2 \frac{\| \frac{\partial V}{\partial x} G \|^2}{\epsilon} + \| \frac{\partial V}{\partial x} G \| \delta^{\max} \leqslant \frac{\epsilon}{4}$, for all values of $\| \frac{\partial V}{\partial x} G \| \delta^{\max}$, has been employed. The bound given in (C.11) allows for using theorem (B.10) and (B.11) to conclude that, after some time, the norm of the state vector $\|\tilde{x}\|$ bounded by a class $\mathcal{K}$ function of ϵ. Therefore, choosing $\epsilon \to 0$ small enough ensures that $\|\tilde{x}\|$ is also small. A more detailed introduction to Lyapunov redesign techniques can be found in [17].

References

[1] ITER Physics Basis 1999 Chapter 1: Overview and summary *Nucl. Fusion* **39** 2137
[2] Joffrin E. 2007 *Plasma Phys. Control. Fusion* **49** B629–49
[3] Wijnands T., Houtte D.V., Martin G., Litaudon X. and Froissard P. 1997 *Nucl. Fusion* **37** 777
[4] Suzuki T. *et al* 2005 *AIP Conf. Proc.* **787** 279
[5] Ferron J.R. *et al* 2006 *Nucl. Fusion* **46** L13
[6] Moreau D. *et al* 2008 *Nucl. Fusion* **48** 010401
[7] Ou Y., Xu C. and Schuster E. 2010 *IEEE Trans. Plasma Sci.* **38** 375
[8] Ouarit H., Brémond S., Nouailletas R., Witrant E. and Autrique L. 2011 *Fusion Eng. Des.* **86** 1018
[9] Shi W. *et al* 2012 A two-time-scale model-based combined magnetic and kinetic control system for advanced tokamak scenarios on DIII-D *51st IEEE Conf. in Decision and Control* 4347–52
[10] Boyer M. *et al* 2013 *Plasma Phys. Control. Fusion* **55** 105007
[11] Maljaars E., Felici F., de Baar M.R., van Dongen J., Hogeweij G.M.D., Geelen P.J.M. and Steinbuch M. 2015 *Nucl. Fusion* **55** 023001
[12] Wehner W. *et al* 2016 Predictive control of the tokamak q profile to facilitate reproducibility of high-$q_{\min}$ steady-state scenarios at DIII-D *2016 IEEE Conf. on Control Applications (CCA)* 629–34
[13] Boyer M.D., Barton J., Schuster E., Walker M.L., Luce T.C., Ferron J.R., Penaflor B.G., Johnson R.D. and Humphreys D.A. 2014 *IEEE Trans. Contr. Syst. Technol.* **22** 1725
[14] Argomedo F.B., Witrant E., Prieur C., Brémond S., Nouailletas R. and Artaud J.-F. 2013 *Nucl. Fusion* **53** 033005
[15] Vu N.M.T., Nouailletas R., Lefèvre L. and Felici F. 2016 *Control Eng. Pract.* **54** 34
[16] Barton J.E. *et al* 2015 *Nucl. Fusion* **55** 093005
[17] Khalil H. 2001 *Nonlinear Systems* (New Jersey: Prentice Hall)
[18] Barton J., Shi W. *et al* 2013 Physics-based control-oriented modeling of the current density profile dynamics in high-performance tokamak plasmas *52nd IEEE Int. Conf. on Decision and Control* 4182
[19] Pajares A. and Schuster E. 2016 Safety factor profile control in tokamaks via feedback linearization *55th IEEE Conf. on Decision and Control* 5668
[20] Pajares A. and Schuster E. 2018 Nonlinear robust safety factor profile control in tokamaks via feedback linearization and nonlinear damping techniques *2nd IEEE Conf. on Control Technology and Applications* 306
[21] Hinton F.L. and Hazeltine R.D. 1976 *Rev. Mod. Phys.* **48** 239
[22] Sauter O., Angioni C. and Lin-Liu Y.R. 1999 *Phys. Plasmas* **6** 2834
[23] Erba M., Aniel T., Basiuk V., Becoulet A. and Litaudon X. 1998 *Nucl. Fusion* **38** 1013
[24] Buttery R.J. *et al* 2019 *J. Fusion Energy* **38** 72